ROBUST STRAIN MEASUREMENT ON DEFORMATION-ROUGHENED MICROSCOPIC SURFACES WITH FLUORESCENT MARKER IMAGING

by

Mona Raeissi

B.S., Mechanical Engineering, Tabriz University, 2015

Submitted to the Institute for Graduate Studies in
Science and Engineering in partial fulfillment of
the requirements for the degree of
Master of Science

Graduate Program in Mechanical Engineering

Boğaziçi University

2018

ACKNOWLEDGEMENTS

I want to thank my family for their endless love during my life. They have always believed in me and this has always been my greatest motivation in my life. My dad, Majid Raeissi, has always encouraged me to continue my graduate studies. He always gives me the unconditional support that helped me to stand on my own. Special thanks to my angel, my mom, Malihe Nasrollahi Azad, who has dedicated all her life to our family without any expectation. For me, she is the complete meaning of being a nice human. Without her unconditional kindness and patience, I would never be the person I am now. I also thank my little sister, Homa Raeissi, for always being there for me with her positive energy and sympathy. I always wish that I can achieve many things to make them proud of me.

I would like to express my gratitude to my thesis supervisor Prof. Can Aydiner for his guidance, advise and support throughout my study. It was a valuable experience that I have had the opportunity to work under his supervision. I would also like to thank to my thesis committee, Prof. Gülin Vardar and Prof. Alpay Oral for accepting to read my thesis and for their valuable comments.

I am grateful to my lab mates Nima Shafaghi, Buğra Ücel, Necdet ali Özdür and Enver Kapan for their kind helps and supports during this study. I am also grateful to my dear friends Gülcan Özerim and Asal Kharazi for their precious support and sharing my hopeless times during this study and special thanks to my dearest, Mehrdad Ghanbari Azar, for being beside me in all ups and downs of this study with his complete support, trust and kindness.

This work was in part supported by the Scientific and Technological Research Council of Turkey (TÜBİTAK), Grant No: 114M215 and B.U. Research Fund at Bogazici University under contract 15A06M1.

ABSTRACT

ROBUST STRAIN MEASUREMENT ON DEFORMATION-ROUGHENED MICROSCOPIC SURFACES WITH FLUORESCENT MARKER IMAGING

Digital image correlation (DIC) implemented at microstructural length-scales of materials with microscopic imaging has emerged as an important tool to investigate the fundamental mechanisms of deformation. An important problem in the optical implementation of microscopic DIC is the fact that deformation itself can create surface features. These compromise the DIC pattern used for tracking material subsets and cause errors and invalidations. A strategy to overcome DIC invalidations on deformation-roughening structures is to create a deformation mode that filters the microstructure out of the images and simply tracks introduced tracing particles. In this study, fluorescent microscopy is investigated as a viable imaging method to achieve this goal. Fluorescent pattern application has been developed with spraying and spin-casting techniques using both fluorescent DAPI (4',6-Diamidino-2-Phenylindole, Dihydrochloride) solution and fluorescent beads. Beads that are spread on the surface with spin casting yielded consistent patterns that act sufficiently robust in DIC method. In the in situ loading experiments, fluorescent imaging (FDIC) line has been used in parallel to a routine optical microscopy line that has the same magnification to precisely determine and quantify the benefits as well as limitations of the fluorescence application. Two material configurations of as-cast and extruded Magnesium, both intended to favor formation of large twins, has been used in these in situ microscopic DIC+FDIC experiments. The results show that the premise of the FDIC method is viable, namely, while DIC is invalidated in certain twinned material neighborhoods, FDIC maintains producing consistent results.

ÖZET

DEFORMASYON NEDENIYLE BOZULMUŞ MİKROSKOPİK YÜZEYLERDE, FLÜORESAN İŞARETLEME İLE GÜÇLÜ GERİNİM ÖLÇÜMÜ

Mikroskobik görüntüleme ile malzemelerin mikroyapısal uzunluk ölçeklerinde uygulanan dijital imge korelasyonu (DIC), deformasyonun temel mekanizmalarını araştırmak için önemli bir araç olarak ortaya çıkmıştır. Mikroskobik DIC'nin optik uygulamasındaki önemli bir problem deformasyonun yüzey bozulmasına sebebiyet vermesidir. Bunlar, malzeme veri alt kümelerini izlemek için kullanılan DIC modelini riske sokar ve hatalara ve geçersiz verilere neden olur. Deformasyon nedeniyle bozulan yüzeylerin üzerindeki DIC geçersizliklerinin üstesinden gelmek için bir strateji, mikro-yapıyı imgelerden ayıran ve sadece yüzeye uygulanmış DIC desnini izleyen bir deformasyon modu yaratmaktır. Bu çalışmada, bu hedefe ulaşmak için floresan mikroskopisi canlı bir görüntüleme yöntemi olarak incelenmiştir. Söz konusu materyal, yerinde görüntülenen Magnezyum AZ31 olarak seçilmiştir. Floresan desen uygulaması, hem floresanlı DAPI çözeltisi hem de floresan parçacıkalrı kullanılarak püskürtme ve spin kaplama teknikleriyle geliştirilmiştir. Spin kaplayıcı ile yüzeye yayılan floresan parçacıklar, DIC yönteminde yeterince güçlü desenler vermiştir. Yerinde yükleme deneylerinde, floresan uygulamasının sınırlamalarının yanı sıra faydaları kesin olarak belirlemek ve nicelleştirmek için aynı büyütmeye sahip rutin optik mikro- skopi hattına paralel olarak floresan görüntüleme (FDIC) hattı kullanılmıştır. İki dökme ve ekstrüde Magnezyum, bu in situ mikroskopik DIC+FDIC deneylerinde kullanılmıştır. Sonuçlar, FDIC yönteminin öncülüğünün uygulanabilir olduğunu göstermektedirler, yani yük arttıkça DIC ikizlenme şeritlerinin etrafında geçerliliğini yitirirken, FDIC tutarlı sonuçlar elde etmektedir.

TABLE OF CONTENTS

LIST OF FIGURES

LIST OF TABLES

LIST OF SYMBOLS

C	Correation coefficient of DIC
u	Displacement along x-axis
v	Displacement along y-axis
ϵ	Infinitesimal strain component
ϵ_M	Infinitesimal nominal strain
ν	Poisson's ratio
σ	Stress
ω	Infinitesimal rotation component

LIST OF ACRONYMS/ABBREVIATIONS

CCD	Charge Coupled Device
DIC	Digital Image Correlation
EDM	Electrical Discharge Machining
FDIC	Fluorescent Digital Image Correlation
HCP	Hexagonal Close-packed
SEM	Scanning Electron Microscopy

1. INTRODUCTION

1.1. Background

1.1.1. Digital image correlation

Digital image correlation (DIC) is a deformation/motion measurement method which has been developed in 1980s in South Carolina University [1] . DIC is a full field, non-contact technique, applicable on any material (wood, fiber, metal foam, rubber, etc.). This flexible technique is routinely applied in conjunction with the standard material tests, e.g., tensile, torsion and bending tests. Good accuracy, high spatial resolution, versatility, being fast and economical can also be mentioned among benefits of this method. The technique is based on the comparison of the digital images of the deformed and undeformed configuration of the sample surface [2]. Applying the technique over an array of subsets yield high spatial resolution. Unique tracking of the subsets rely on a DIC pattern applied with various methods on the surface of the specimen. The tracking is numerically implemented by DIC algorithms that yield subset displacements and their gradients.

In the area of solid mechanics, deformation fields are usually determined at the macro-scale. However, recent focus is on smaller length scales (nano-scale, micro-scale) to provide a fundamental constitutive description of materials. DIC does not have an inherent length scale and thus is suitable for all length-scales, only depending on the image acquisition technique. To use DIC for the micro-scale deformation measurement, the digital images need to be obtained from high-magnification imaging systems such as an optical microscope or a scanning electron microscope (SEM) [3].

1.1.2. Microscopic DIC

The advancing ability in manufacturing small-sized (micro and nano) components in various fields of engineering, increases the need of experimental investigations to measure the mechanical characteristics at corresponding length scales. In addition, investigation of routine materials (e.g., polycrystalline metals) at microstructural length scales have gained importance for the purpose of formulating more fundamental constitutive relations. To provide the data necessary for both type of investigations, strain needs to be measured at micron and sub-micron length scales [4]. Conventional strain measurement methods, e.g. strain gauges, extensometers, are not suitable for such measurements. Hence, micro-scale use of DIC has recently undertaken a large role in such investigations. There are broadly two types of imaging at this scale: DIC with optical microscopy that offers $5-50\mu m$ resolution and DIC with a scanning electron microscope (SEM) whose resolution can be two factors higher (e.g., [5], [6]).

DIC provides strain fields and microscopic DIC application provides fields at the microstructural levels. The spatial resolution directly describes strain heterogeneity, namely, the non-homogeneous accommodation of strain in the microstructure. Strain heterogeneity is high when strains localize around microstructural features (e.g., grain boundaries). Strain heterogeneity at microstructural scales is tightly connected with material damage and failure. Surface roughening, loss of structural stability and necking during metal forming operations [7] are among its potential undesirable outcomes. Therefore, a comprehensive understanding of strain heterogeneity can significantly improve our ability to design against failure.

All polycrystalline materials exhibit strain heterogeneity at microstructural length scales, including the highest symmetry FCC metals [8] that deform with a single slip system family. However, strain localization levels are significantly more pronounced in hexagonal closed packed (HCP) materials such as Titanium (Ti), Zirconium (Zr) and Magnesium (Mg) due to their compound micromechanical behavior

with multiple slip and twin systems. Efstathiou *et al.* [9] characterize the microstructural deformation of titanium with multiple magnifications, comparing strain maps in different optical resolutions, using ex-situ DIC. Barkia *et al.* [10] study deformation heterogeneity in commercially-pure titanium. In their study, the strain maps are computed using the SEM images recorded during tensile tests along both RD (rolling) and TD (transverse) directions. Padilla *et al.* [11] consider the relation between deformation heterogeneity and local texture in zirconium with in situ optical DIC. Manuel marya *et al.* [12] investigate the ductility and the strength variations in three microstructurally-different (1, single phase, fine grains. 2, two phases, coarse grains. 3, grain boundary precipitates.) Mg alloys, using microscopic DIC. Martin *et al.* [13] quantify strain heterogeneity in a Mg alloy which has a slip dominated deformation mechanism during tension test in microscopic scale using DIC and considers the factors which play significant role in intergranular strain localization, such as local neighborhood orientation of a grain beside its own orientation and other deformation mechanisms occurring at the same time.

Recent microscopic DIC investigations on HCP Magnesium has been undertaken at the laboratory where the current investigation has been conducted, namely, Mechanics of Advanced Materials Laboratory, Department of Mechanical Engineeiring, Bogazici University. Aydiner and Telemez [14] consider rolled Magnesium AZ31 (3wt% Al, 1wt% Zn). Microscopic DIC is implemented on the entire surface of a gradually strained compression sample. In this study, area scanning of the microscope over the sample surface has yielded full-field deformation maps in subgrain resolution. The influence of twining in the deformation behavior of Mg-AZ31 is also emphasized. The sample is loaded in a sense that produces profuse tensile twinning (In- plane compression). The fact that large tensile twins in magnesium cause widespread DIC invalidations has been first observed in their study (details in next section). Later, as an extension of this effort, the grain size dependence tensile-twin-dominated Mg-AZ31 deformation has been studied in the masters thesis of Sevinç Uçar [15]. One of the specific advancements in this study has been to incorporate the ability of geometric filtering. This allowed independent analysis of a specific region in

the overall microscopic DIC results, specifically targeting the shear bands mediated by the tensile-twin avalanches. Kapan *et al.* [16] implemented a DIC study at macroscopic resolution. However, it encompassed a large parameter space that included cyclic loading (compression-tension-compression) as well as rolled and extruded textures of Mg-AZ31. The texture comparison shows that texture is a dominant factor on microstructural deformation heterogeneity. Samples of both textures have similar stress-strain curves, which would make them appear identical in conventional design procedures, but the character of respective strain localizations have been observed to be vastly different.

1.1.3. DIC invalidations in microscopic measurement

The DIC strain measurement error is a combination of experimental errors (detector noise, light variations, vibrations in the system, etc.) and limitations of the algorithm. The total error can be characterized with no-strain rigid body translation experiments. Simply, in these, strain is ideally zero, and non-zero strain will directly characterize the error levels. Typically, the standard deviation of the full-field strain data is taken to be the error of the DIC measurement [14] .

However, the DIC measurement at times totally fails rather than yielding a value with uncertainty. A particular case in microscopic measurements is when DIC pattern itself is corrupted/altered with deformation. Invalidation occurs when slip traces and twin bands emerge in the deformed image and modify the subset pattern extensively with respect to the reference image. Consequently, the tracked intensity signature of the subset is basically lost. Note this issue can arise even when the initial pattern is perfectly adequate. Moreover, even when the DIC correlation does not fail at a particular subset, a strong bias error might be introduced by such pattern alteration.

In the Magnesium deformation microscopic DIC measurements at the Mechanics of Advanced Materials Laboratory, it was observed that the material surface

images were exposed to microstructural alterations. This made microscopic DIC invalidations typical statistical occurrences for these materials. The physical reason that the deformation disrupts the micrographs particularly acutely in Magnesium is the activation of deformation twinning in these materials. Twins are band structures that suddenly emerge in crystallites with transformed crystallographic orientations. The (tensile) twins in Magnesium not only reach large volume fractions (sometimes consuming entire grains) but they also have large individual sizes. Consequently, the twin disruptions in images are significantly more dominant than traces caused by slip, which is the more common form of plasticity in crystalline metals. Grain scale extrusions and intrusions caused by twinning and their sizes can be obtained with white-light interferometry which provides precise details of the surface topography. Hazeli *et al.* [17] have measured the size of surface extrusions and intrusions caused by twinning on the surface of a cylindrical specimen of magnesium AZ31. Upon imposing 1% strain, these surface deformations are found to be in [-500,400] nm range. This step size is easily sufficient to cause DIC pattern corruption for typical microscopic magnifications. Figure 1.1 shows the appearance of new twin bands in grains of rolled Magnesium AZ31 alloy with 50 μm grain size, from reproducer [14]. The emerging twin bands invalidate the DIC analysis as signified by the disappearance of the strain map at their location. In this study, since the maps are overlaid over deformed images; emerging twin bands appear as culprits of the lack of data.

1.1.4. Strategies for overcoming DIC invalidations

In electron microscopy, recent literature reports one method of dealing with the pattern corruption issue in DIC. Combination of in-situ scanning electron microscopy (SEM) with optimized microscopic digital image correlation (μ-DIC) is a method to overcome various challenges associated with concurrent mapping of the deforming microstructure [18]. The novelty of the method is the possibility of selective microstructure-independent pattern imaging and selective pattern-independent microstructure imaging conditions which are achieved by the optimization of SEM imaging conditions. So, basically, one SEM mode records a specially grafted carbon

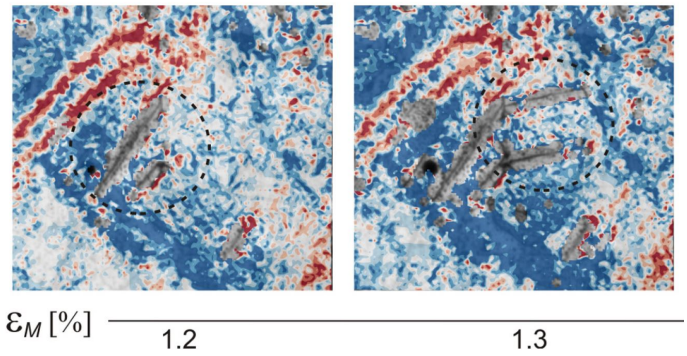

Figure 1.1. The appearance of (additional) twin bands in Magnesium with increasing nominal strain. Strain maps are overlaid over deformed images. (Reference images do not contain the twin bands.) [14]

tracker particle (DIC speckle pattern) layer on the microstructure. This imaging mode omits the microstructure from the image and therefore, omits any problems with microstructure alteration described in the previous section.

Optical imaging, the technique we will utilize in this study, has naturally completely different physics compared to electron microscopy. Hence, formulating a mode that expunges the microstructure out of the image would require a different method. This study proposes fluorescence microscopy to accomplish this aim. In fluorescence mode, only fluorescent tracker particles will be recorded in microscopic optical imaging. This idea's application in DIC has been scarce. Particularly, no studies in the category of mechanical loading experiments with in situ microscopic DIC has been implemented within our knowledge. A nanoscale fluorescence microscopy DIC experiment is done on polymeric structure (PDMS) in the literature, but it is a different study that does not have a loading component [19]. The paper does not aim to overcome the DIC invalidation due to surface roughening; it rather gives a technical account of the pattern quality achieved in this mode. They coin the acronym FDIC to stand for fluorescenceDIC, which is also adopted in this thesis.

1.1.5. Fluorescent microscopy

Fluorescence is defined as the absorption of light with a specific frequency (energy) and emission of light with a lower frequency (energy). Fluorescence excitation occurs between two main levels of electron energy bands. Electron of a fluorescent particle in ground state becomes excited after absorbing a light with a specific frequency which pushes to a higher level of energy. After fluorescence lifetime, a photon is radiated with the energy equal to the energy difference of the two levels as shown in Figure 1.2, thus, the electron is relaxed in ground state. Since the emitted fluorescent light has less energy and therefore a longer wavelength than the excitation light, the two can be easily discerned with adequate filtering.

Fluorescent dyes and particles are used in flow visualization and measurement techniques [20] and the heaviest utilization of them is in biology and biomedical sciences. Fluorescent imaging is a non-destructive technique to track or analyze biological molecules using fluorescence microscope [21]. Fluorescence microscope is a microscope that is specialized to sift the response of fluorescent species from the response of the remaining material. This is possible since the fluorescent species emits a lower energy of light while the rest of the material primarily responds with the excitation energy. The sample is illuminated with high intensity light that is at the excitation wavelength of the fluorescent particles. Over the reflected wavelengths, the much weaker emission response of the fluorescent particles are filtered. Thus, in a properly configured microscope, only the fluorescent-emitted light should reach the detector. This results in an image composed of fluorescent structures observed with high contrast over a dark background. The limits of detection are generally governed by the signal to noise ratio which is the effectiveness of filtering the reflection of remaining structures from the image. Fluorescence effect ends when the light source stops acting on the fluorescent material. Fluorophores have the ability of radiating numerous photons through the cycle of excitation and emission.This process can be repeated until the fluorophores are damaged such that the above-mentioned cycle becomes irreversible. The intensity reduction of the fluorescent materials during this

cycle is called photobleaching which plays a significant role in fluorescent imaging applications. (See section 4.4.)

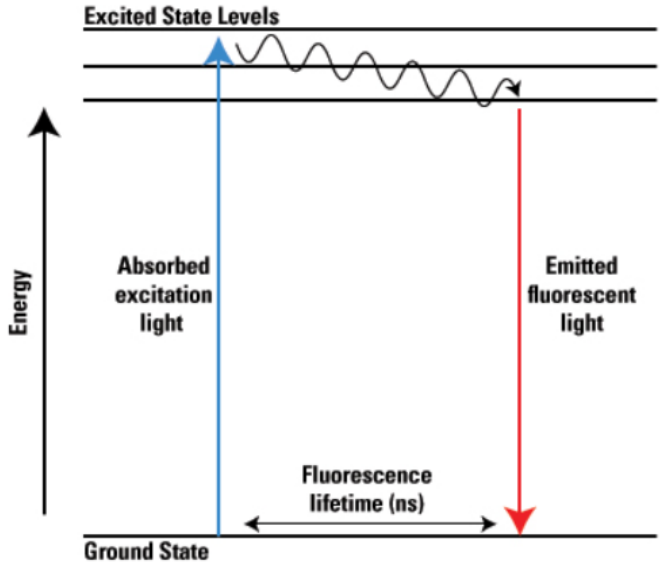

Figure 1.2. Jablonski energy diagram of fluorescence

1.2. Aim and scope

This study investigates on the use of fluorescence microscopy in addition to regular microscopy during in situ loading experiments to allow robust strain mapping of deformed metal surfaces specially at the existence of the surface roughening at the microstructural length scale. Fluorescence microscopy provides an imaging mode that eliminates the microstructure from the images. This in turn eliminates microstructural image corruption issue in DIC implementation when DIC is applied on microstructure images. Furthermore, in this study, the investigation is also on fluorescent dye application as a sufficiently robust DIC pattern. Simply, in each experiment, the comparison of regular microscopy and fluorescent microscopy during in situ loading is conducted under same conditions and with one sample that its surface is coated with fluorescent particles. This fluorescent patterns plays the role of normal DIC pattern under regular microscopy (without any UV-light exposed on the surface) and it fluoresces under UV-light source eliminating all the signals ex-

cept fluorescent particles, making a fluorescent pattern. The study will take place in Mechanics of Advanced Materials Laboratory as a new modification for the existing setup as fluorescent microscopy and the aim is to develop the DIC technology to be more robust specially in the regions where microstructure modifications can cause DIC invalidation under regular microscopy.

Development of the FDIC application requires a fluorescent microscopy line. The essential elements required for fluorescent microscopy line (see section 4.1) is procured and the line is introduced to the already existing microscopy line.

Selection of fluorescent dye and fluorescent nano particles for micro DIC and FDIC pattern application is one of the significant steps in this study. At first steps of the study, a water based fluorescent solution called DAPI is picked as the dye for elementary fluorescent pattern application. Various methods are used for dye application on the sample surface. Preparing different concentrations of the fluorescent solution for patterning with spray-gun, with spin caster and direct application on the surface are the examples of the methods implemented in this study for patterning. In the advancing steps fluorescent nano particles in different particle sizes are purchased. The properties of the nanoparticles and their advantages over DAPI are explained in detail in section 4.2. These particles are also applied with spray-gun and spin caster as two succeed methods to achieve FDIC pattern with sufficient levels of consistency. In section 4.3, the FDIC pattern application and pattern tests are explained. Overcoming the photobleaching effect of the particles during the experiment is also one of the significant challenges in this study. During the developments of the proposed method, the problem is tried to be overcome. The photobleaching phenomenon is explained in section 4.4.

In the selection of the appropriate material configuration, large and easily visible twin structures have been the main criterion. During the progression of the thesis, two configurations have been considered. In the first stage, an as-cast batch of Mg AZ31 that has very large grains (grain size around 1 mm) have been considered. The

idea behind this configuration has been that, with the huge parent grains, the twin band structures that emerge in them would be large and easily detectable. Figure 1.3 shows the combined micrographs (at 0.8% strain, 7x15 scan of 400 μm frames) of a precursor experiment where regular scanning microscopic DIC has been implemented to spot the *targeted* DIC invalidation problems. These are exemplified in Figure 1.4 and DIC invalidation at the large twin bands are evident. However, statistical significance in terms of observed grain numbers has been an issue with the very large grain size of this sample.

To circumvent this problem, extruded Mg AZ31 that has been given an in-house annealing treatment to allow 30 μm grain sizes has been considered. Aside from ideal grain size, previous experiments have ensured that DIC invalidation has been a huge issue for this material as well. Heavy activity of tensile-twin is ensured with the texture-load combination, i.e., extruded Magnesium compressed along extrusion direction. The widespread invalidations are depicted in Figure 1.5, adopted from a previous experiment, where the sample is at -2 % over its tensile-twin plateau. Twin activities that cause modifications and accordingly DIC invalidations on the surface of the sample are shown with yellow arrows.

In summary, the potential benefit of using FDIC over twinning zones will be evaluated using an as-cast and an extruded configuration, the latter providing the statistical element required in the study. The DIC and FDIC strain analysis of two implemented experiments are given in chapter 5.

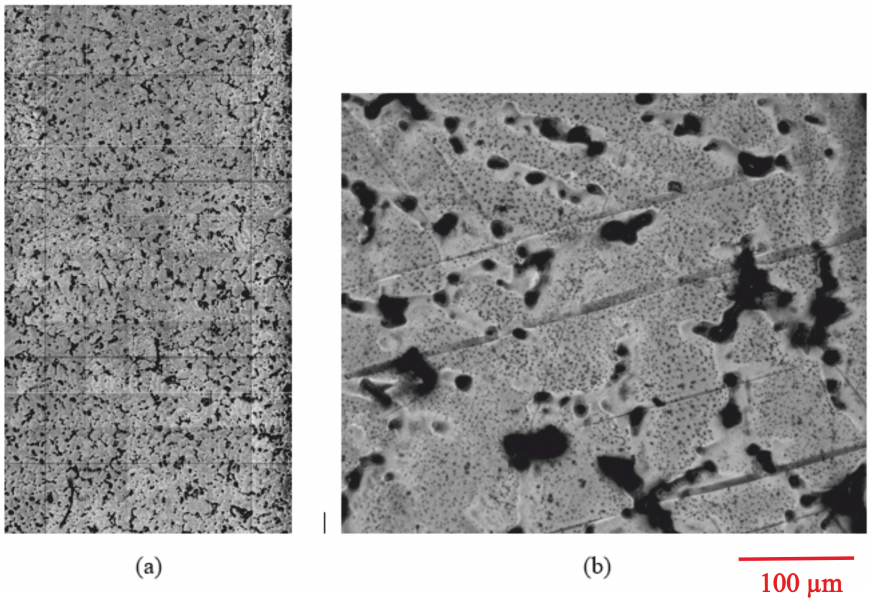

Figure 1.3. Appereance of large twin bands at 0.8% tensile strain. a) micro-DIC grid of the Mg-Az31 as cast sample. b) one frame including large twin bands.

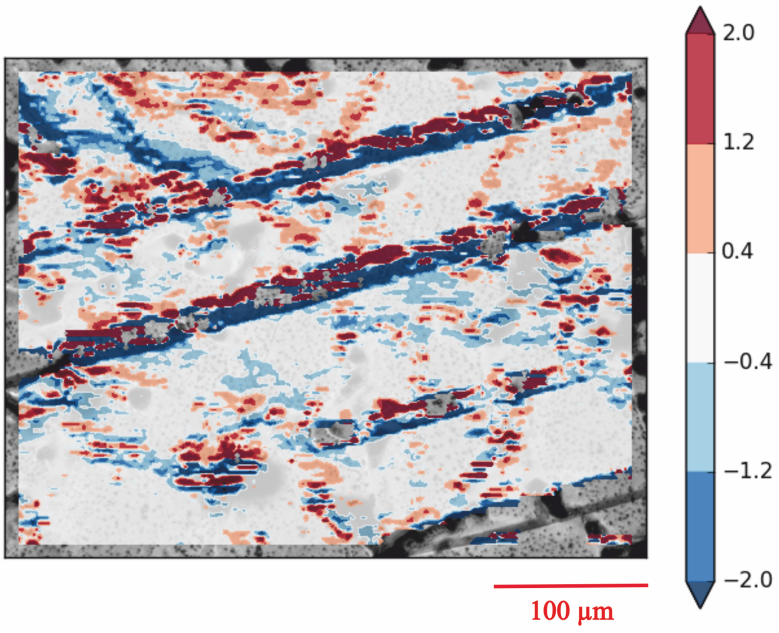

Figure 1.4. DIC invalidations on twin bands of Figure 1.3(b).

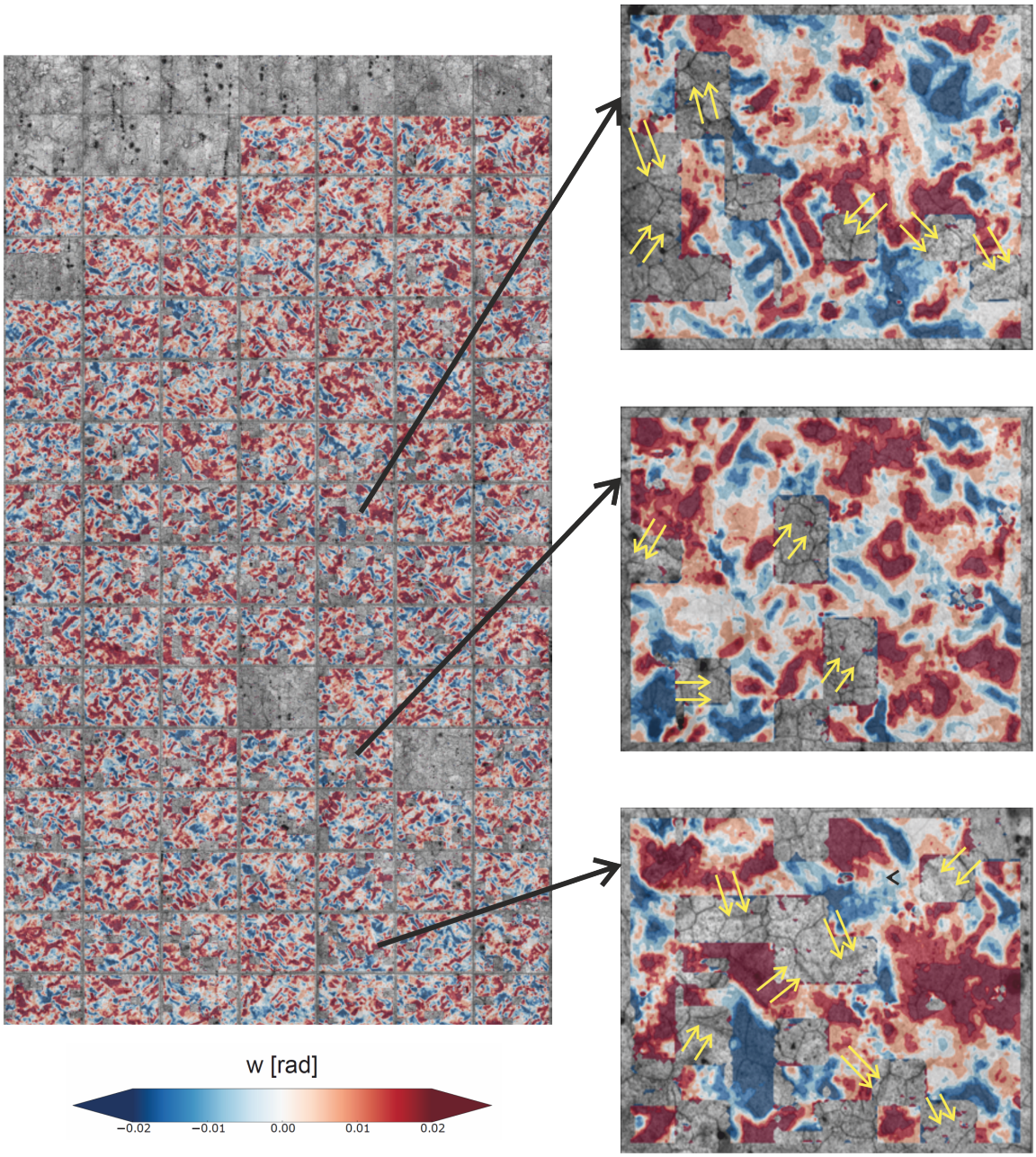

Figure 1.5. DIC invalidations are observed on twin bands activated in -2% strain. Yellow arrows show the activated twin bands on the sample surface causing a significant surface roughening. accordingly the disappearance of the strain map in those regions is observed.

2. EXPERIMENTAL METHODS

2.1. Digital image correlation

Digitial image correlation (DIC) technique is capable of measuring the displacement field on the surface of a loaded sample with high spatial resolution. The method works by comparing the digital images of the surface recorded at undeformed and deformed states of the sample. High spatial resolution comes from tracking closely spaced points on the surface. Tracking is implemented by tracking the intensity signature of the points. Tracking a single pixel in the two images is not possible due to uniqueness issues. More precisely, a pixel will have an intensity value in the range of [0,255] (in the most typical 8-bit gray scale image) and tracking a value in the deformed image will return many results, not to mention the fact that tracking the exact intensity can be quite unreliable given the uncertainty in experimental conditions. To render the tracking unique, correlation considers subsets of the image, typically in square shape centered about the neighborhood of the targeted point. These are called DIC subsets. Subsets should be large enough to be present a unique intensity distribution that can be tracked. However, they should also be as small as possible to maximize the spatial resolution. Therefore, the ideal subset size is the smallest one that is still trackable.

This study used first order subsets that has six search parameters that are optimized as the subset defined on the reference image is located in the deformed image. These parameters are the displacements (u, v) and displacement-derivative values $(\frac{\partial u}{\partial x}, \frac{\partial u}{\partial y}, \frac{\partial v}{\partial y}, \frac{\partial v}{\partial x})$ defined at the subset center. Figure 2.1 exemplifies a frame that shows DIC subsets and grid points. The parameters at each subset are determined by optimizing a correlation coefficient. The correlation coefficient defines the error between the intensity distribution over the subset in the reference image and the intensity distribution over the search domain at the deformed image. Least-squares type intensity error summed over the subset pixels is typical and utilized here. Opti-

mization algorithms also vary but the standard Newton-Raphson method works well for successful DIC patterns and adopted at the fine search stage [22]. Since arbitrary deformation carries reference subset pixel centers to subpixel locations in the deformed image, intensity values at the deformed image have to be estimated in between the pixels. This requires interpolation whose order and type are also important for the success of the DIC implementation. Bicubic spline performs much better than the bilinear interpolation [22] and adopted in the DIC algorithm of this study (Figure 2.2) . Mathematical detail of the DIC algorithm is provided in Section 3.

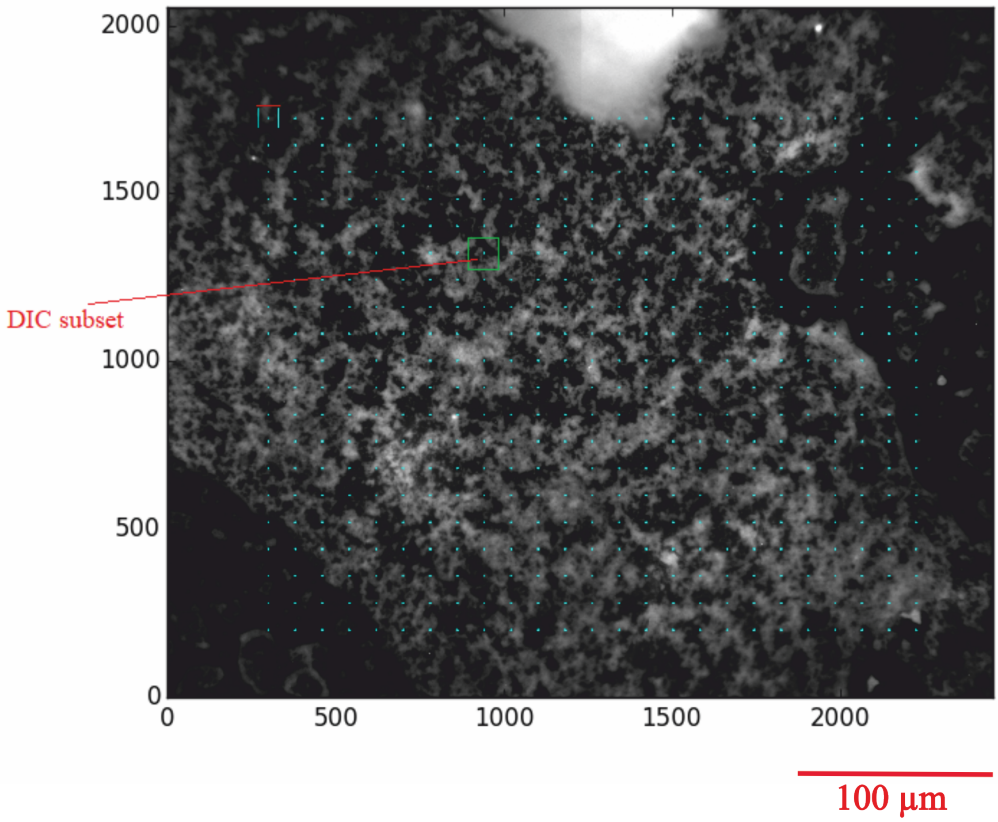

Figure 2.1. A DIC frame with grid points that each of them is a center point of a DIC subset on a fluorescent patterned Mg-AZ31 surface.

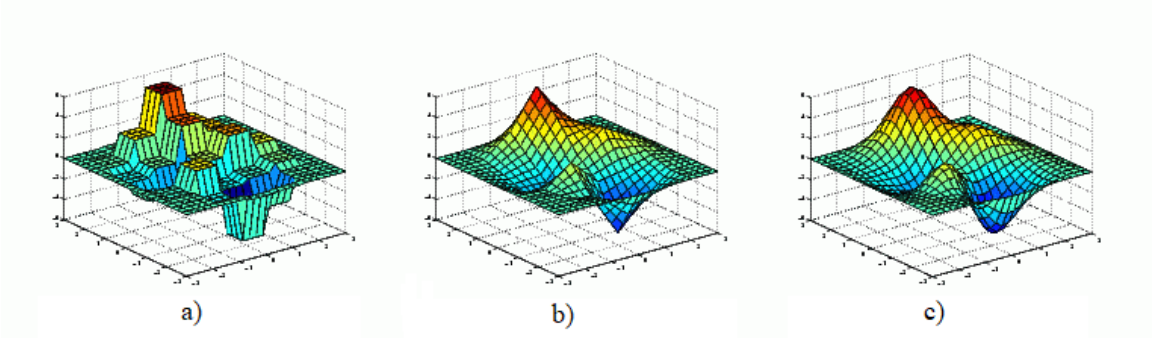

Figure 2.2. Comparison of different interpolation methods. (a) nearest neighbor, (b) bilinear, (c)bicubic spline.

2.2. Sample geometry and surface prepration

Scientific investigations that utilize microscopic DIC benefit from the identification of the grain boundaries in order to relate the strain fields with the underlying microstructure. Therefore, adequate metallographic processing of the sample is typically desirable and part of the sample preparation in micro-DIC experiments. Metallography does not only provide local information about the shape and the location of the grain boundaries but also statistical information, e.g., the average grain size. Hardness of the metal is a critical parameter that governs the ease of the metallography processes for a particular metal. It is typically harder to polish softer metals to a satisfactory degree. Magnesium and its light alloys are soft metals (modulus 45 GPa, yield strength 100 MPa) and require a delicate operation in this regards. The metallography process consists of five major steps: sectioning, mounting, grinding, polishing, chemical etching.

- Sectioning: The samples used in this study are dog-bone shaped Mg-AZ31 samples that are extracted from the parent material with wire electric-discharge machining (EDM). Wire-EDM is a non-traditional cutting method that particularly allows the machining of complex shapes. It cuts through the formation of numerous electrical sparks between the wire-electrode and the sample. These

sparks melt the sample locally and facilitate cutting. Figure 2.3 shows the geometry of the sample in detail.

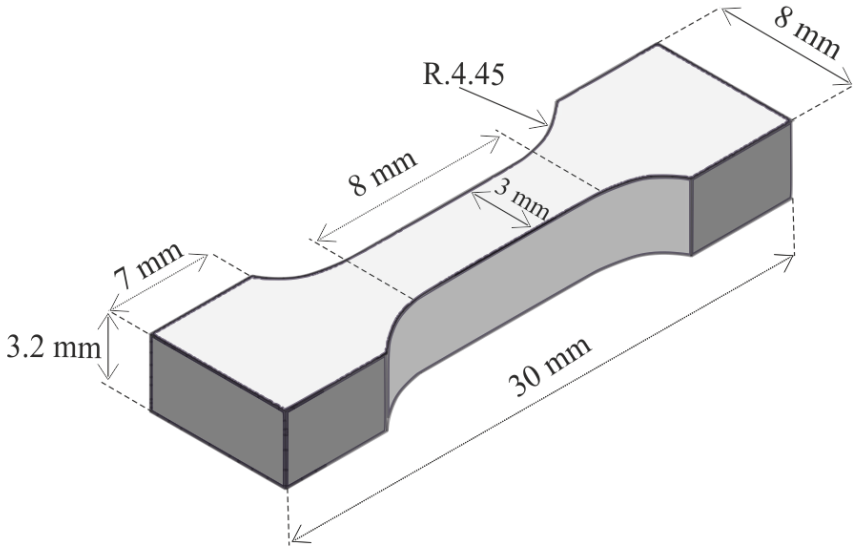

Figure 2.3. Sample geometry and dimensions.

- Mounting: Small dog-bone specimens are hard to handle during metallography steps. Mounting allows proper support during grinding steps and protects the specimen from bending. It also helps to avoid distortion of the soft Magnesium surface, which is critical for DIC imaging. At the utilized microscopic resolution a high level of flatness is required such that the entire image can be in focus. The mounting mixture is composed of cold mounting powder and fluid, which is intentionally chosen as the kind that dissolves in acetone. Their relative proportion is 2:3. After preparing the mixture, it is poured slowly into a flexible plastic mounting mould (5 cm in diameter) in which the dog-bone shaped Mg-AZ31 specimen is placed. The mounted specimen is then allowed to dry for 20-30 minutes in ambient air. The mount mixture is dissolved after the grinding stage in an ultrasonic bath with acetone while the surface is protected with a clear tape from the damage of acetone. Polishing (that entails very limited material removal) and etching steps follow.
- Grinding: In this step, all surface features and scratches introduced in previous processes (such as cutting) are removed. The surface is progressively abraded

with abrasive grinding papers classified according to their grit sizes. The most common abrasive paper for grinding metals and polymers is made up of silicon carbide (SiC). Here, p1000, p1200, p2500 is used for experiment samples starting from low to high grades. Low grade papers contain relatively coarse particles with fewer grits in bigger diameters in comparison to higher grade abrasives which are shown in table 2.1. Grinding direction, load and the speed of grinding can influence the flatness of the specimen. Surface removal is high in grinding with low P-grade papers. So the time of these steps should be kept sufficiently low and be increased with upcoming steps with high p-grade but not more than 10 minutes for each step. At the end of the last step (p2500), the aim is to remove all scratches from the sample surface. At the end of each step, the sample surface is washed thoroughly with water to clean remnant large particles that can cause deep scratches in the next stage. With the soft Magnesium, very low pressure is applied on the mounted sample at all stages to reduce the possibility of scratches as well as pre-deformation on the sample surface.

Table 2.1. Particle size and common grit size in abrasive paper

European (P-grade)	**Standard grit**	**Median diameter (micron)**
P1000	500	18.3
P1200	600	15.3
P2400	800	6.5

- Polishing: The purpose of polishing is providing a mirror-like and deformation-free surface with no scratches on it. Mechanized polishing is performed on Mg alloys which is more time-efficient than manual polishing. A polishing cloth is placed on the horizontal surface of the rotating polisher used in low speeds (150-200 rpm). Colloidal silica which is a dilute solution of very fine particles of silica in water, is the proper polishing solution for Mg alloys according to the literature [23]. At the end of the step, remnant silica from the surface is removed with the ample application of ethanol. Because of the low resistance of Mg alloy to corrosion, using water causes a rapid oxidation in the surface.

Therefore, in the polishing step, the washing liquid is switched to ethanol. Before the etching step, the surface is examined under optical microscope. All the remaining scratches can be identified before etching and one should try to remove all the scratches specially in the gage section of the sample since these will be visible on the microscopic DIC images.

- Etching: The last step is etching with the purpose of bringing out the microstructure (grain boundaries, grain shape, grain size) of the polished specimen under microscope. Chemical etching, the most common method for etching metals, is used in this study. Numerous formulations are being used as an etchant solution for Mg alloys. The recipe for our etchant is 0.64 g picric acid, 1ml pure water, 15ml ethanol, 1ml acetic acid. The surface is submerged in the prepared etchant solution for 3-10 seconds. When selecting the etching time, not to risk the need to repolish, under-etch is more preferable than over-etch. If the surface is insufficiently etched, one can submerge the surface to the etchant further. Once the grain boundaries are revealed with etching the sample is ready to be applied a DIC speckle pattern. Out of two chosen materials, the as cast sample of of Mg-AZ31 alloy has large grains which can be observed even with human eye. Figure 2.4, shows the revealed microstructure (grains and grain boundaries) of this sample after chemical etching.

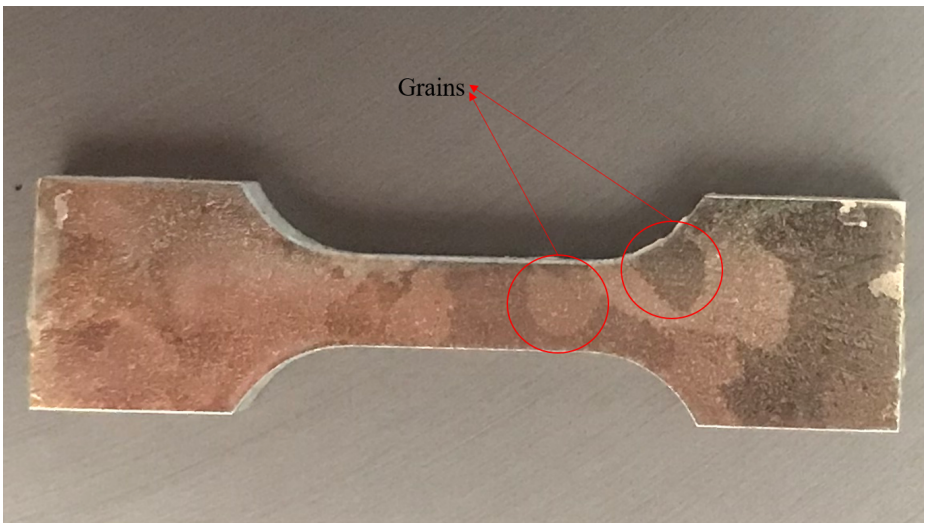

Figure 2.4. Mg-AZ31 as cast batch's surface after chemical etching.

- DIC Speckle Pattern Application: DIC tracking works through the signature of the intensity pattern. Therefore, a high-quality DIC pattern is the most important factor in the success of a DIC implementation. Sufficient levels of intensity, contrast and random pattern signature are required for the comparability of the images. It is ideal if the surface has a non-repetitive, isotropic, high-contrast, non-periodic, and consistent pattern. Moreover, the speckles have to be in proper length scale, i.e., at the proper proportion to the DIC subset; speckle size about one fifth the subset size is considered ideal. For macroscopic DIC applications, proper speckle patterns for DIC are easily formed by spray painting black dots over a white background. However, creating the optimized DIC patterns for micro-scale measurements, with the requirement that the grain boundaries should still be visible (so the surface should not be coated), is challenging. There are cases though when etching features provide sufficient tracking signature for the microscopic DIC. In many cases, though, the surface features are not sufficient. So, consistent DIC patterns are required to be applied externally. Various techniques have been studied to develop DIC pattern at optical-microscopy scales (roughly micron-sized speckles) such as airbrush paint-spraying, gold web imprinting, application of chemical depositions and finally fluorescent nano particles. [24–26]. Figure 2.5, shows a pure Nickel grain structure before and after the application of paint layer prepared in the current laboratory.

The typical application of the microscopic DIC pattern in the Mechanics of Advanced Materials Laboratory utilizes a precision Iwata airbrush. The typical paint solution contains 2 drops of Iwata black dye diluted in 3 ml distilled water. Two important factors in air brushing the dye on the surface of the specimen is the spraying pressure and the distance of the air brush from the sample. The optimized distance has been found to be 10cm which avoids coarse speckles caused by too close a distance and inappropriate speckle sizes caused by too far a distance. The optimum pressure is found to be 4 bars. The air brushing time also plays an important role in achieving a consistent pattern. Air brushing for more than 4-5 seconds start to coat the surface

while less than 2 seconds is a short time for achieving a pattern with sufficient levels of signature to be tracked.

In this FDIC investigation, developing the capability to apply the fluorescent pattern at the correct length-scale is a significant part of the challenge. Application of the pattern has been attempted by using two base forms. The first form is fluorescent dyes which is in fluid form and is sprayed over the surface. The second form is microscopic beads, called fluo-beads in this study. These are chemically infused fluorescent particles that are in disc morphology. The experiences with each are described in detail in sections 4.2 and 4.3.

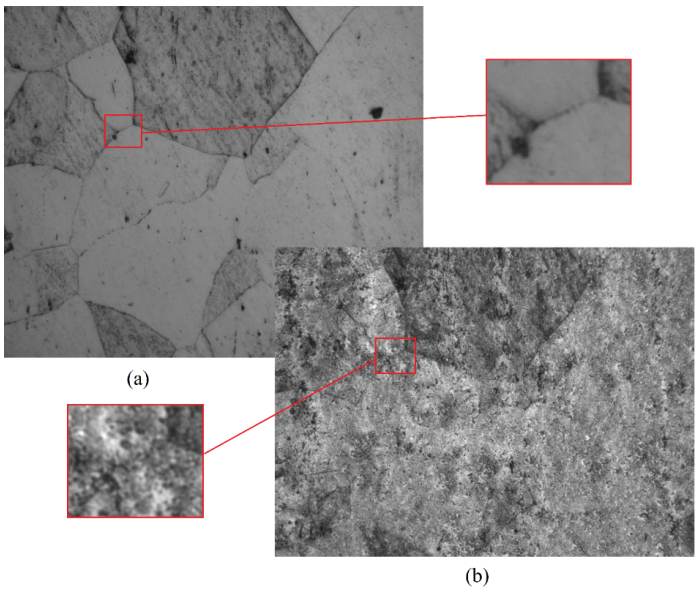

Figure 2.5. Pure Nickel grain structure under the 20x microscope (a) before and (b) after the application of the paint-based speckle layer. The shown sub-regions show the intensity variation with higher magnification. The subset in part (b) clearly has a far superior signature for DIC deformation measurement.

3. NUMERICAL ANALYSIS

3.1. DIC algorithm

DIC method is based on the comparison of the intensity data in DIC subsets of the deformed and undeformed digital images. In the ideal case, and if the subsets were merely translated with respect to each other, the intensity values of the same subset in deformed and undeformed image would match. In practice, they do not exactly match because of the deformation of the loaded specimen as well as experimental errors.

The two subsets are correlated with each other through the minimization of a "matching error measure". The error measure here is least squares type.

$$C = \sum_{i=1}^{N} [F(x, y) - G(x^*, y^*)]^2 \tag{3.1}$$

where, F(x,y) is the gray level value at (x,y) in undeformed image and G(x*,y*) is the gray level value at (x*,y*) of the deformed image. Two points are related to each other by the deformation occurred on the surface. Where u is the displacement for the subset center in x direction and v is the displacement of the subset center in y direction.

$$x^* = x + u(x, y) \tag{3.2}$$

$$y^* = y + v(x, y) \tag{3.3}$$

The coordinates of an arbitary point in the subset of a deformed image with a grid point of (x_0,y_0) can be approximated with a first order Taylor equation as below. where, Δx and Δy are the distances of the subset center to the point in which the DIC measures are calculated.

$$x^* = x + u(x_0, y_0) + \frac{\partial u(x_0, y_0)}{\partial x}\Delta x + \frac{\partial u(x_0, y_0)}{\partial y}\Delta y \tag{3.4}$$

$$y^* = y + v(x_0, y_0) + \frac{\partial v(x_0, y_0)}{\partial y}\Delta y + \frac{\partial v(x_0, y_0)}{\partial x}\Delta x \tag{3.5}$$

The search to minimize the error measure is conducted with Newton–Raphson optimization and considers a first-order deformation of the subsets. Grid points are the centers of the DIC subsets where the correlation is implemented. Here, the calculated DIC parameters are u, v, $\frac{\partial u}{\partial x}$, $\frac{\partial u}{\partial y}$, $\frac{\partial v}{\partial y}$, $\frac{\partial v}{\partial x}$ that are defined at the subset centers.

The first order spatial derivatives at the subset centers are used for a better fit to the displacements at the subset center. These are not equated to the corresponding strains since the more accurate practice is to take numerical derivative of the displacements over the DIC grid. As such the normal strain in x direction at a subset (i,j) in the DIC grid is defined by

$$\epsilon_{xx}^{i,j} = \frac{\partial u^i}{\partial x} = \frac{u^{i+1,j} - u^{i-1,j}}{2\,\Delta} \tag{3.6}$$

according to the central difference formula where Δ is the grid spacing. Other strain and in-plane rotation (ω_{xy}) formulas follow accordingly and we will merely

mention their generic form

$$\epsilon_{yy} = \frac{\partial v}{\partial y} \tag{3.7}$$

$$\epsilon_{xy} = \frac{1}{2}(\frac{\partial u}{\partial y} + \frac{\partial v}{\partial x}) \tag{3.8}$$

$$\omega_{xy} = \frac{1}{2}(\frac{\partial u}{\partial y} - \frac{\partial v}{\partial x)}) \tag{3.9}$$

In this study, subset size is fixed at 61 x 61 pixels ($\sim$ 12 μm x 12 μm) and the distance between the subset centers (grid points) is 20 pixel ($\sim$ 4 μm).

3.2. FDIC quality measures

In both regular microscopic DIC and FDIC investigations, the reliability of the DIC pattern is measured by quality-check codes written in python. For this purpose, two images of the same local frame is grabbed consecutively. Since, no deformation is imposed and translation is limited to any that is imposed by system vibration, the displacement histograms indicate the systematic error which consists of algorithmic and experimental errors (the camera noise of the CCD detector). One can utilize the strain histograms in the same manner as well, whose ideal values are fixed at zero given the lack of deformation. In the comprasion of consecutively grabbed images, the ideal result in displacement (or strain) is a Dirac-delta function. However, even the camera noise of the CCD detector, introduces errors which prevents this ideal histogram with no distribution. The ideal error distribution is a bell-shaped single of Gaussian character. However, if the pattern is weak and the measurement noise dominates the signal, false results can be produced that appear as outlier peaks about the central peak. As shown in Figure 3.1, the red curve represents the difference

histogram of two images which are taken back to back with a good pattern and the blue curve represents the histogram of images with bad pattern in which there is a wide and intermittent distribution of the data points.

Figure 3.1, shows the microscopic DIC benchmark (subset size 61x61 pixels, AVT Pike cameras with Sony ICX625 sensors) in a properly-patterned pure nickel surface. The standard deviation of u in this image is 0.050 pixels (0.01 mm). With a grid spacing of $20 pixels$, this points to strain uncertainty of 2.5×10^{-3}. This is typically what can be hoped for strain accuracy for these measurement parameters. The microscopic DIC analysis is in this frame with this pattern. In all the experiments, after patterning, the surface pattern is quality checked and the displacement histograms with standard deviations around 0.050 pixels represent adequate patterns from the quality point of view for DIC and FDIC investigations.

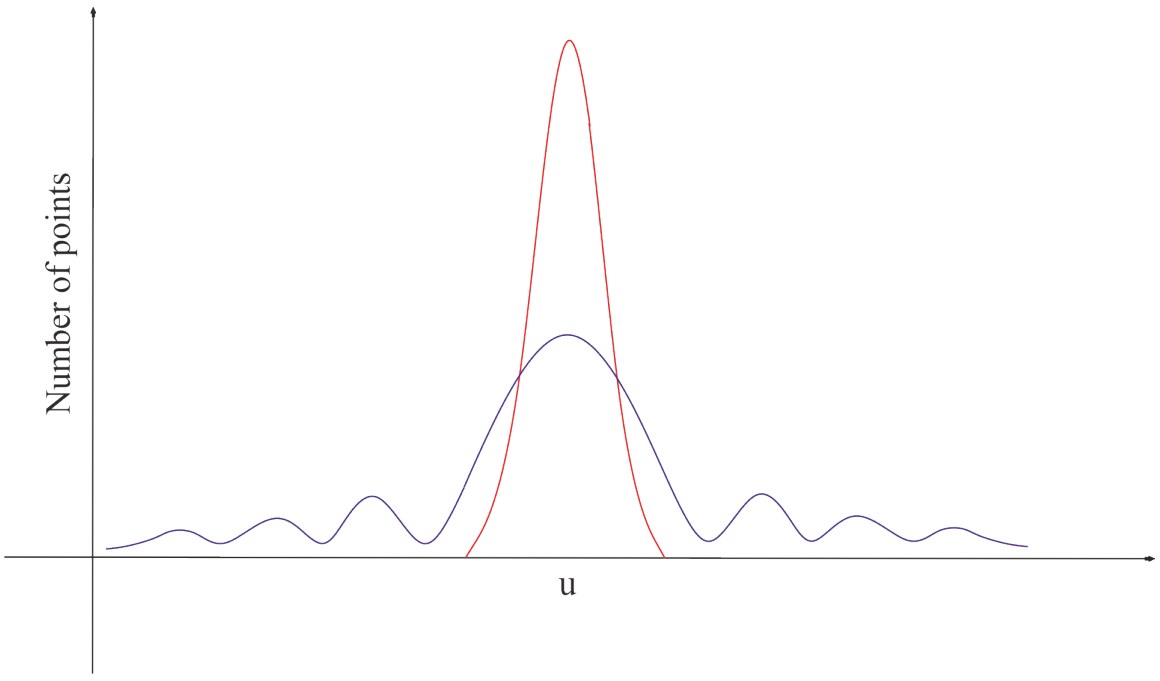

Figure 3.1. The comparison of the intensity difference histogram of a good pattern (red curve) vs bad pattern(blue curve).

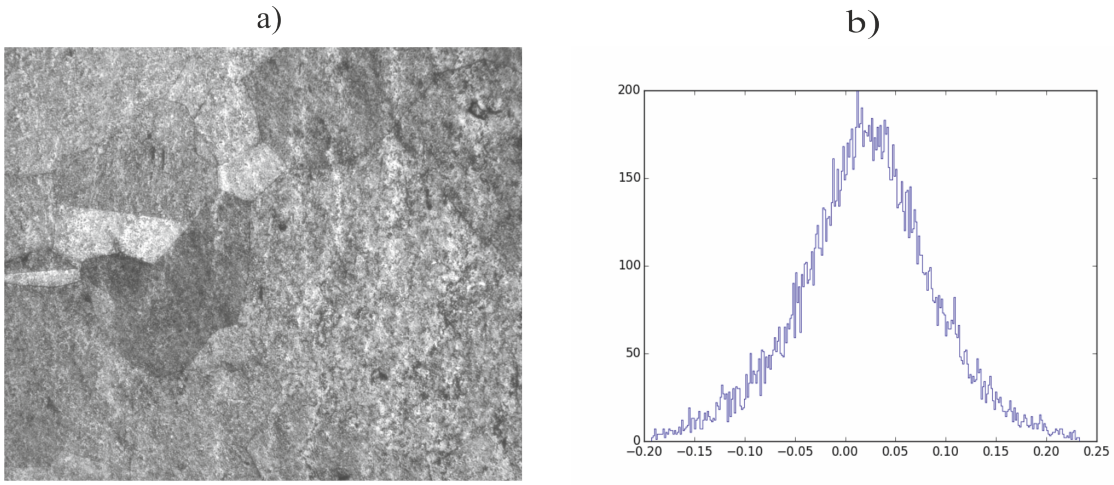

Figure 3.2. Microscopic DIC benchmark of a well-patterned Nickel surface. a) a microscopically patterned pure Nickel. b) histogram which indicates displacement in x direction(u) in two consecituvely grabbed images.

4. DEVELOPMENT OF FLUORESCENT DIGITAL IMAGE CORRELATION APPLICATION

4.1. Setup

The most typical configuration used in the in situ multiscale DIC experiments implemented at Mechanics of Advanced Materials Laboratory is shown in Figure 4.1. This configuration utilizes two parallel optical lines for macroscopic and microscopic imaging. The optical lines are attached to the aluminum U-frame, placed on a vibration isolation table. The cameras in the shown lines are AVT Pike F505B, with 5 Megapixels Sony ICX625 CCDs. These cameras are also used in testing the as-cast Magnesium AZ31, the initial material of this study. While working on the second material in extruded form, a newer camera was introduced to the FDIC line, FLIR Grasshopper with IMX 250, 5 MP CMOS detector. The better sensitivity and signal-to-noise ratio of this camera helped with the low-light-detectin challenge of fluorescent microscopy.

The optics in the micro-DIC line is the tandem of an adapter tube, a Navitar zoom lens and a Mitutoyo infinity corrected objective lens (10x magnification), listed from the camera-end toward the observation surface. The optical resolution is approximately 0.19 $\frac{\mu m}{pixel}$.

In this FDIC investigation, fluorescent imaging line has been introduced as an additional line to the regular in-situ deformation measurement setup as shown in Figure 4.2 while the macroscopic line has been discarded from this configuration. The line on the right is conventional microscopy and the one on the left is the newly added fluorescence microscopy line. In this line, another Mitutoyo infinity-corrected objective lens is used that has 20x magnification (Figure. 4.2(d)) though the overall magnification of the lines are matched using appropriate adapter tubes. Figure 4.3 shows the close up of the fluorescent line and the micro tensile loading frame. A cru-

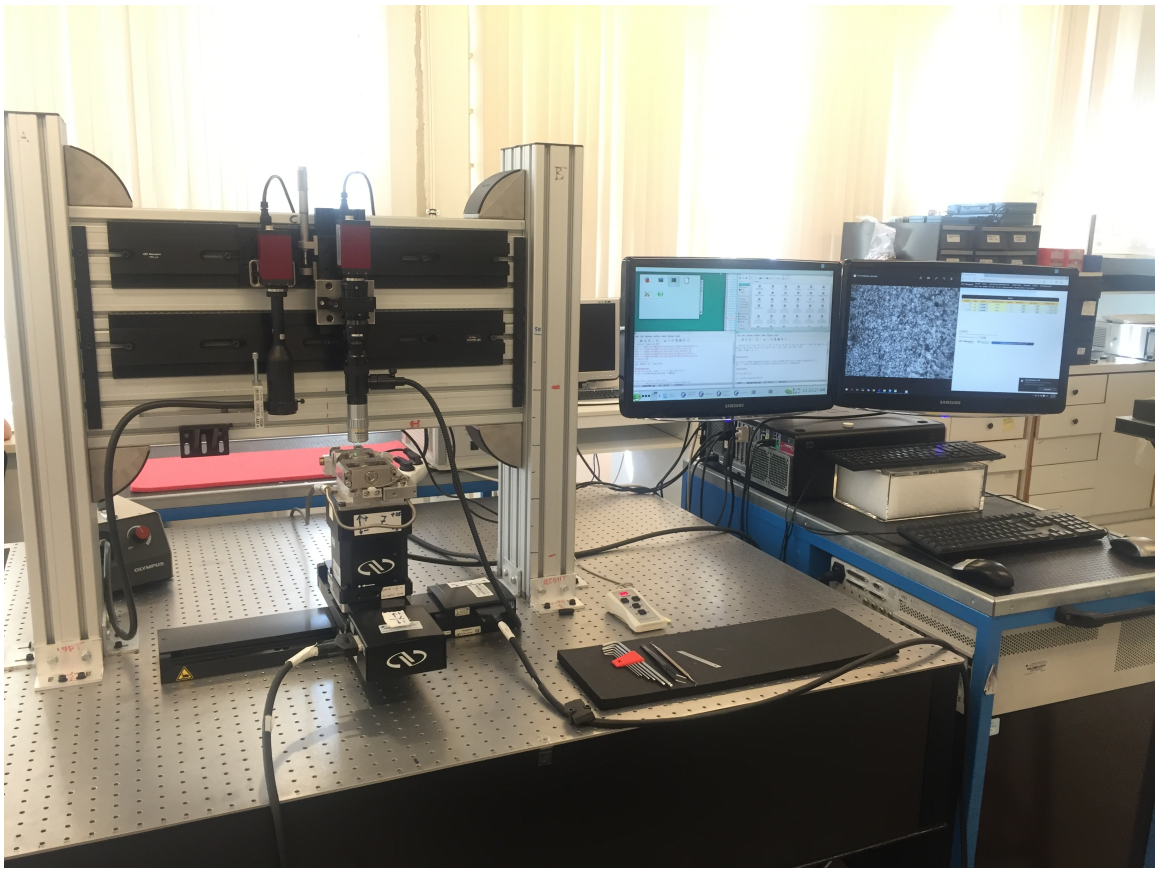

Figure 4.1. Regular in-situ deformation measurment setup.

cial additional element that has been purchased for this investigation is the UV light source (Figure. 4.2(h)) and its light guide (Figure 4.2(g)). In this FDIC configuration, a black-out curtain covers the entire setup all around the table preventing any additional light that would compromise the signal in the fluorescent microscope. The essentially-different elements of the fluorescence imaging line are (i) the filter housing (Figure 4.2(f)) and (ii) the light source(Figure 4.2(h)). The filter cube fits inside the filter housing. Both the excitation light source and the light filter are suited for fluorescent particles used in this study (described in section 4.2). The filter shown in Figure 4.4 contains an excitation filter and an emission filter in an a 90deg arrangement and also a bisecting mirror element in between. The excitation filter separates the specific band of wavelength that excites the fluorescent particle from incoming light waves. The dichroic mirror directs the light to expose the surface. The light reflected from the surface is transmitted by dichroic mirror toward the CCD camera, only once more passing through the emission filter. The emission filter removes light at the excitation frequency only allowing the lower-energy emitted light from the fluorescent particles to pass through. At the end, the image contains only fluorescent particles, because the actual sample's surface reflects the excitation frequency.

4.2. Fluorescent selection

In the FDIC application, fluorescent pattern creates the tracking signal that will be used by the DIC algorithm. Therefore, as with any DIC application, its quality is of utmost importance. Selection and application of fluorescent dyes and particle are the main steps in this process. In this study, two different fluorescent-pattern-application methodologies are attempted. The first utilizes water-based DAPI solutions and the second utilizes Sicastar-BlueF fluorescent nano particles stable in organic solvents. (200 nm ,500 nm, 1 μm). They are excited with ultraviolet light and emit blue hue in visible range. The particles are selected such that their excitation and emission wavelengths are compatible with the filter in the fluorescent microscopy line. The photobleaching rate of dyes under UV-light (as the excitation source) is also a critical factor since the FDIC experiment spreads over a considerable time period. Both base

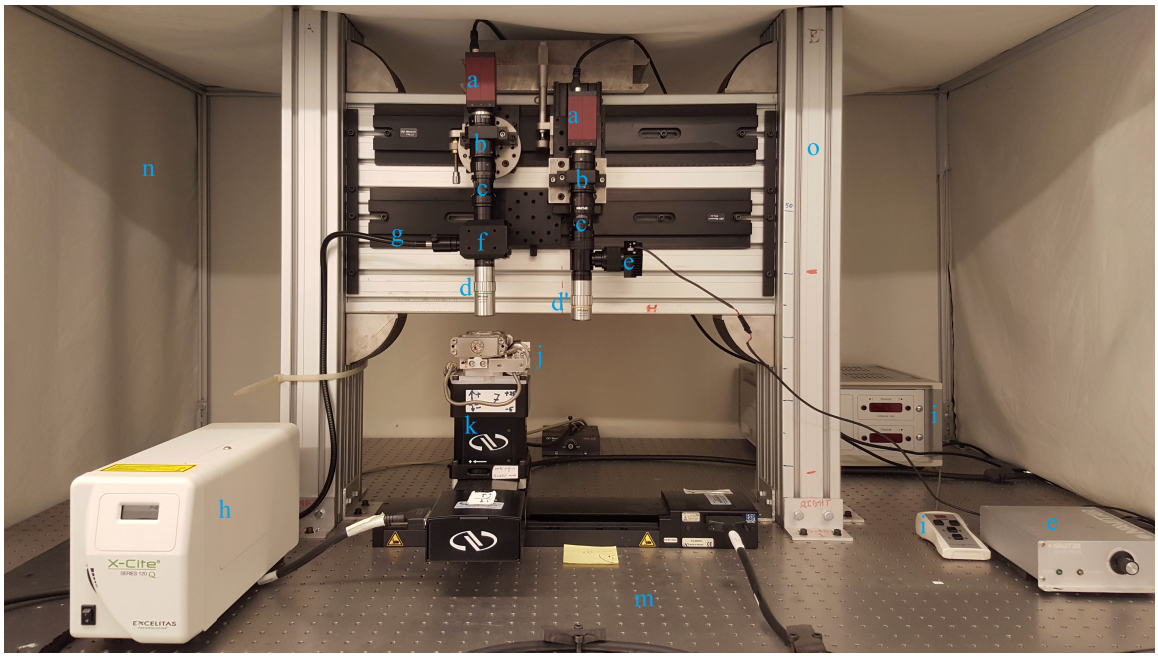

Figure 4.2. Fluorescent and regular microscopic DIC lines for in-situ deformation measurements. (a)CCDs (charge-coupled-device), (b)2x adapters, (c) manual 6x zoom lenses, (d) 20x infinity corrected lens, (d') 10x infinity corrected lens, (e) digital bright light controller(f) fluorescent filter housing, (g) liquid UV light guide, (h) X-Cite 120Q ultraviolet illuminator, (i) loading cell, (j) micro tensile loading frame, (k) Z-stage, (m) vibration isolation table, (n) black out curtain, (o) aluminum frame.

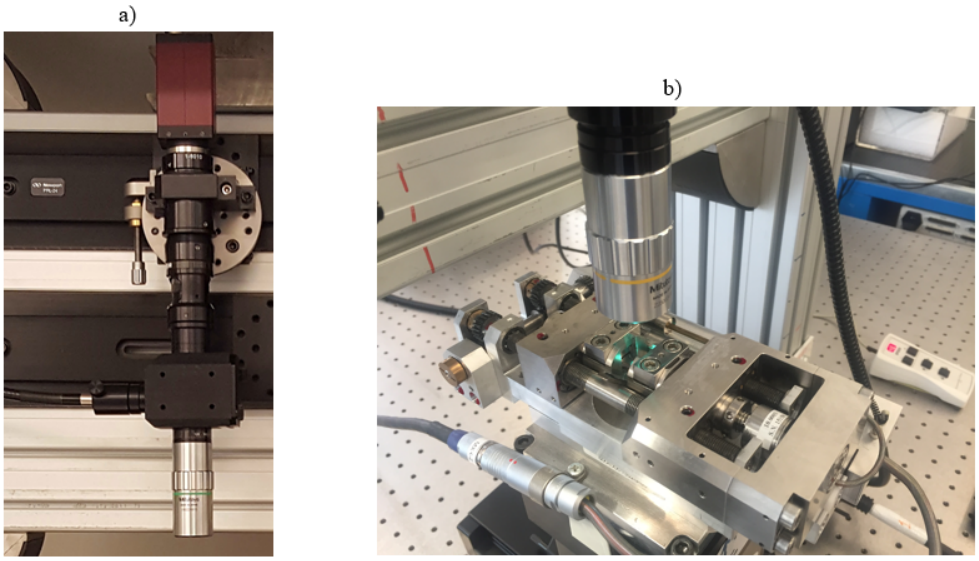

Figure 4.3. Close up of the (a) fluorescent microscopy line and (b) micro tensile loading frame.

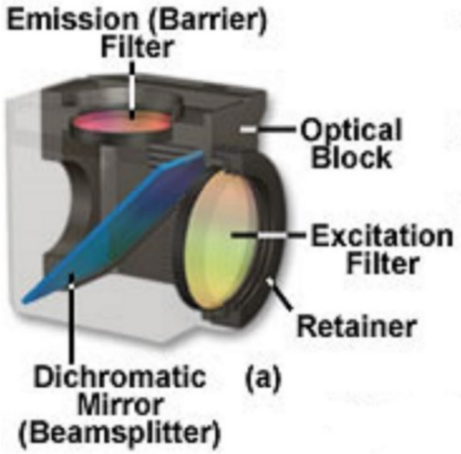

Figure 4.4. configuration of filtering cube.

materials for the pattern, namely, the utilized DAPI solution and the nano particles (beads) have almost the same excitation (354 nm) and emission (450nm) wavelengths (Figure 4.5). Even though DAPI solution and fluorescent beads have similar properties and are exposed to similar conditions in this study, they are obviously different in regard to shape, storage requirements, and photobleaching trends. These aspects are compared in Table 4.1.

Table 4.1. The main differences of DAPI And Fluorescent nano particles.

	DAPI	**Fluorescent particles**
Shape	Stain, not a specific shape	Spherical
Storage	-20°C	Room temperature
Photobleaching	Less resistant	More resistant
Dilution in ethanol	Fluorescent effect is killed	It works

For both DAPI solution and fluorescent beads, several concentrations are prepared for patterning. Various methods were applied in order to achieve consistent patterns in this study. The successful method of patterning that was determined through a process of elimination is explained in next section.

4.3. FDIC pattern tests

Fluorescent patterning in this study is implemented on the surface of Magnesium AZ31 directly to directly assess the feasibility of the patterns in this application. More precisely, the effect of any reaction with the Magnesium AZ31 surface is this way taken into consideration. DAPI solution is sprayed using an airbrush while both spraying and spin-casting (spin coater/caster shown in Figure 4.6) were attempted to spread the beads.

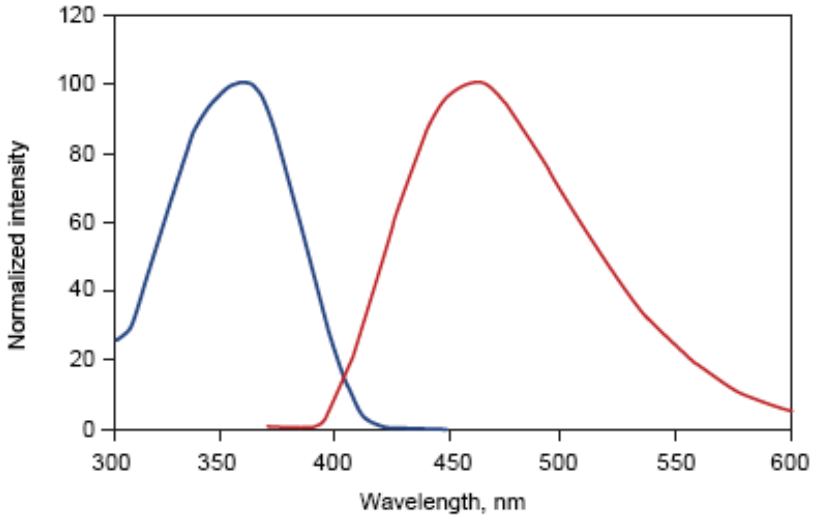

Figure 4.5. Excitation and emission spectra of DAPI. Blue curve is the excitation spectra and red curve is the emission spectra.

Figure 4.6. (a) Iwata air brush, (b) Spin coater (caster).

4.3.1. DAPI Solution pattern application with a spray-gun

Using spray-gun for fluorescent pattern follows the same procedure of pattern application for routine optical microscopy experiments, explained in section 2.3. Several concentrations of DAPI diluted in water (1:100, 1:50, 1:10) from several spraying distances (5-15 cm) were tried. Since, DAPI does not contain spherical particles, most of the time, the pattern was made up of loosely clustered fluorophores with no consistent coverage at the DIC subset scales (Figure 4.7).

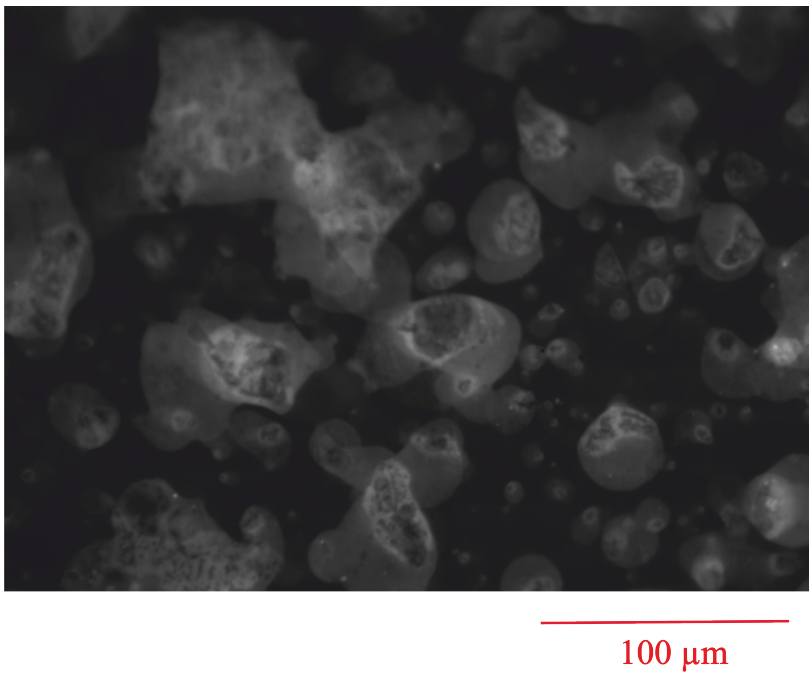

Figure 4.7. Micro image of a DAPI-painted surface using spray-gun.

4.3.2. Bead pattern applied with the spray gun

For bead patterning, spray gun application was attempted with reservations. Since, the particles are 200nm to 1 μm sized spheres, the spray gun could be clogged. To be prudent, low concentrations of beads were used, e.g., 1 mg/ml nanoparticle/100 ml pure water, at first. The spray gun was rinsed carefully after the application to ensure that no particles remain in the nozzle. Gradually increasing the solution's concentration up to 1:10, monodisperse, isotropic and high contrast patterns could

be achieved with this method as shown in the Figure 4.8.

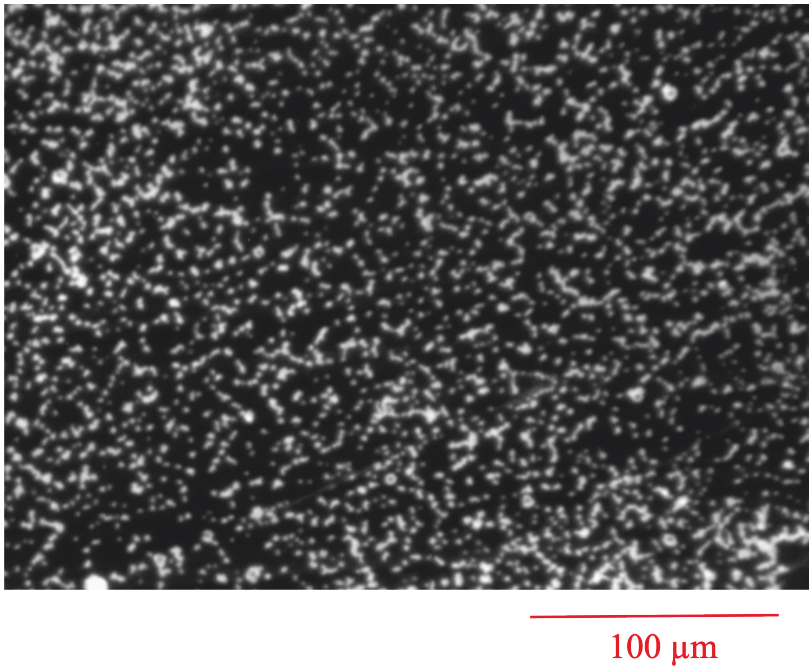

Figure 4.8. Micrograph of a 200nm fluobead applied to Magnesium AZ31 surface using an Iwata spray-gun.

4.3.3. Bead pattern application with spin casting

The other method used in this study is to spin-cast a solution of fluobeads on the sample's surface. The effect of spin coating rate was studied in a range of 700 rpm up to 2000 rpm. Low rates of coating can result in clusters and agglomerations on the surface, while higher rates can simply push the entire material out of the surface. 1400 rpm is observed as an ideal rate for applying a monodisperse pattern. Figure 4.9 shows the Fluo-bead-painted surface of the sample using spin caster.

Sottos *et al.* [19] have implemented this method creating fluorescent silica nanoparticles, labeling with rhodhamine fluorescent dye(555nm excitation wavelength) with blaaderen and Vrij method [27]. They used a 0.1% solution of nanoparticles (nominal diameter 80nm) in ethanol. In their application, this solution has been spin-casted on samples of polydimethylsiloxane (PDMS).

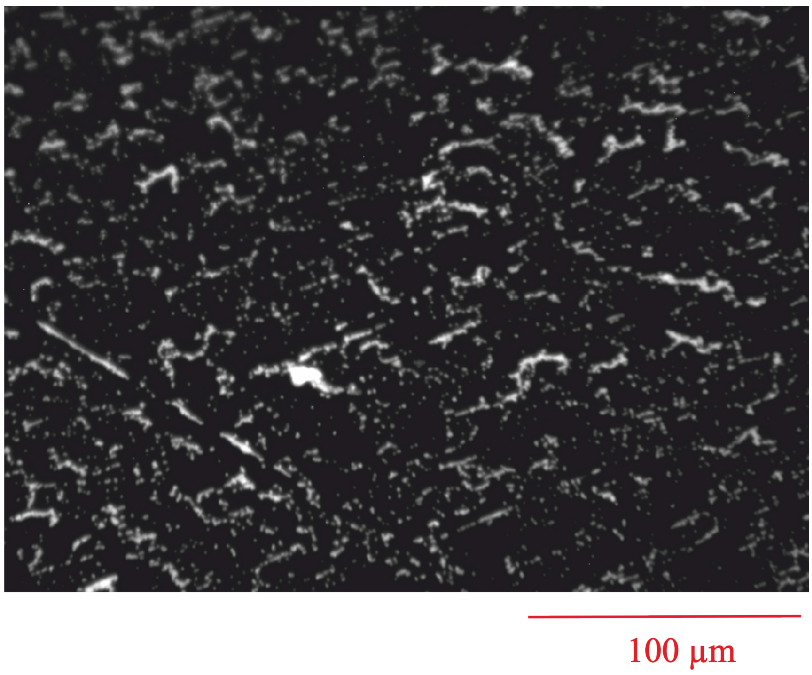

Figure 4.9. Micrograph of a 200nm fluobead-spincoated surface.

4.4. Photobleaching tests

Photobleaching is a dynamic process in which fluorophores lose their ability to fluoresce in time. The photobleaching phenomenon has been a many theme in fluorescence measurement since the 1970s [28]. Light-induced bleaching is a significant phenomenon that takes place rapidly when the fluorescent particles are exposed to high magnification objectives that focus intense light over small localities. Photobleaching is also affected by the excitation frequency and is a bigger problem when high-energy (e.g., UV light) light is used. Long and constant exposure to the excitation source can also be the reason of photobleaching which imposes significant limitations in fluorescent microscopy. Figure 4.10 shows the photobleaching rate of Mg AZ31 sample surface patterned with fluorescent nanoparticles. Here three images are shown, the reference, image after a minute of exposure and image after half an hour exposure. The incident UV light source has been used at maximum intensity for this application. Camera shutter has been fixed at 1 second to ensure comparability. It is clearly seen in Figure 4.10 that intensity histograms shifts left toward

zero intensity due to photobleaching and most of the intensity loss takes place at the beginning, indicating an exponential decay behavior.

In literature, there are studies on reducing the photobleaching phenomenon in cell science [29–32] and it is expressed as an exponential function $I = Be^{-kt}$ [28]. The exact mechanism of photobleaching remains to be a subject of ongoing discussion. Though it is unavoidable, one can limit its effects by

- minimizing the incident light intensity,
- minimizing the length of the time for acquiring an image,
- acquiring nonbleaching fluorescent particles, e.g, laser dyes or dyes with reversible photobleaching cycle [33].

The Figure 4.11 shows the fluo-bead-coated surface of the sample using the spin caster. The images in this figure are recorded with regular time intervals (10s) while the surface is exposed with UV light. The fact that the photobleaching takes place obeying an exponential decay in time is shown in Figure 4.11. This means that, at the beginning of the image acquisition, by exposing the surface to UV-light, the intensity drops rapidly.

In the current loading experiments with in situ FDIC measurement, exposing the surface minimally with the UV-light is an important criterion in the experimental procedure. In this study, proper control of the incident light is done manually. This will be explained in detail in section 5.1.4. By reducing the photobleaching rate to the minimum possible, the DIC errors due to image intensity differences can be also minimized.

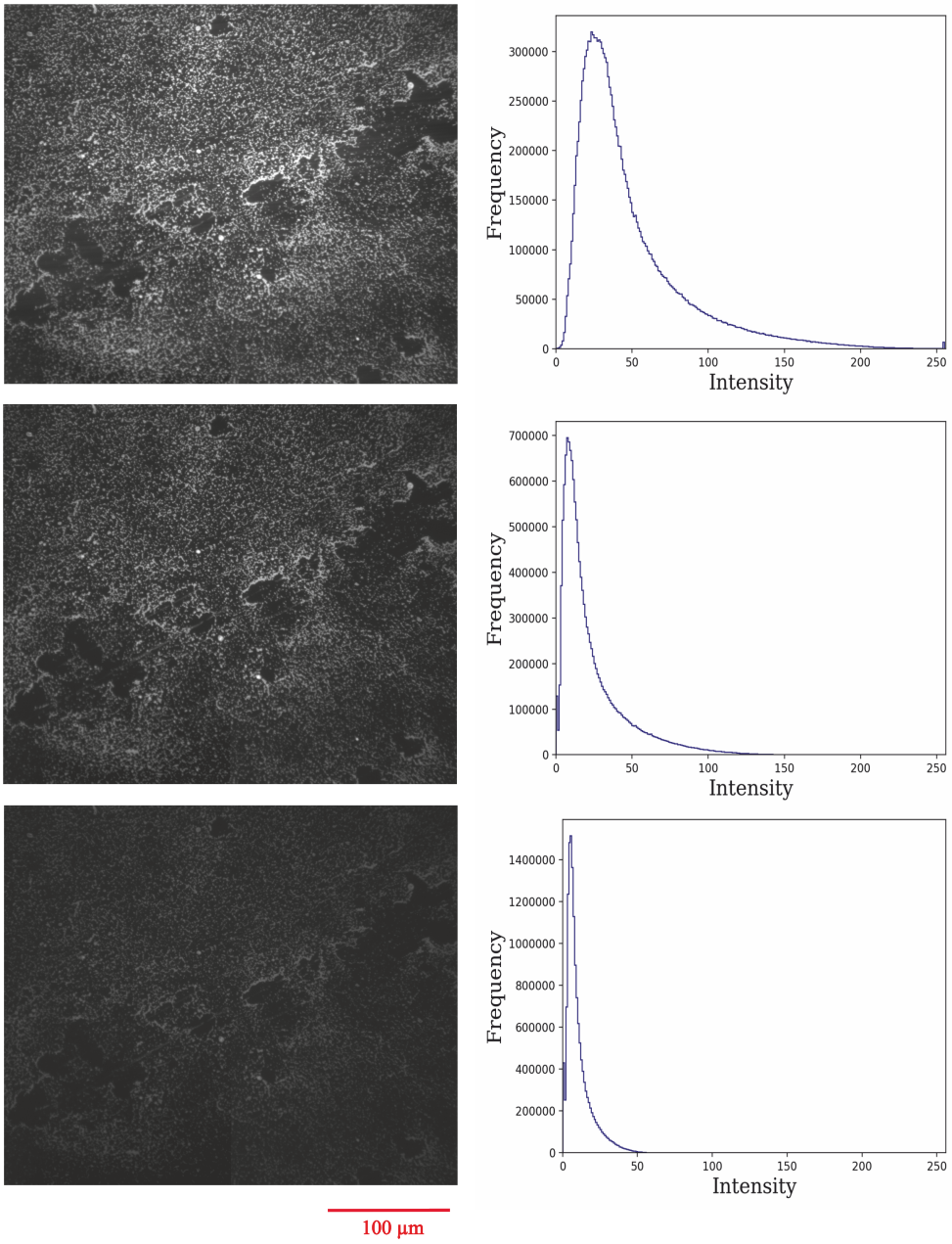

Figure 4.10. Photobleaching on fluorescent patterned sample surface, a) beginning of the imaging. b) after 1 minute, c) after 30 minutes.

Figure 4.11. Photobleachig pace on fluorescent patterned sample surface. The images from (a) to (h) are taken in 10 seconds intervals.

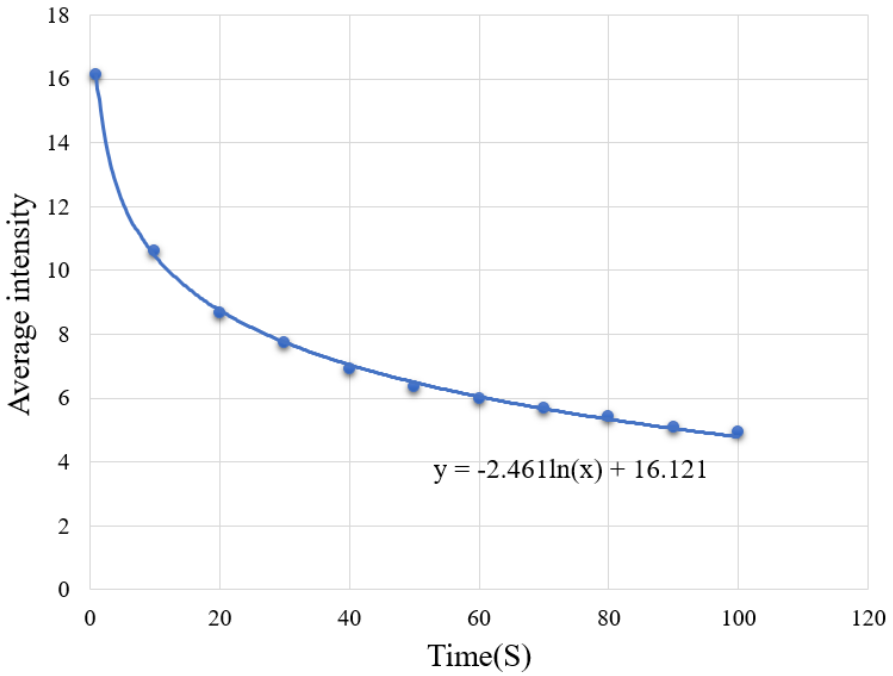

Figure 4.12. Average intensity-Time graph of the images in figure 4.9.

5. RESULTS AND DISCUSSION

Two samples are considered in this investigation. To recap, the first sample is from an as-cast batch of Mg-AZ31 while the second is cut from an extruded and annealed rod. The method has been developed through its first stages utilizing the as-cast sample. The second experiment has been formulated over the experiences of the first one, including the sample choice. It was found that better statistics is necessary to evaluate the potential benefit of FDIC over twinning zones. Therefore, a smaller grain size extruded material has been picked for the second experiment, which provided a 3:1 ratio with grain and DIC/FDIC subset sizes. As-cast and extruded sample experiments will be explained in turn in Sections 5.1 and 5.2. Common sections include 5.1.1 and 5.2.1 that describe the experimental procedure, 5.1.2 and 5.2.2 that describe stress-strain curves, 5.1.3 and 5.2.3 that present surface-roughening performance of DIC and FDIC, 5.1.4 and 5.2.4 that describes photobleaching performance in the FDIC line, and finally, 5.1.5 and 5.2.5 that show strain maps and any material-behavior deductions. The second experiment commands higher statistics that are analyzed via strain histograms. This also provides a quantitative handle on the potential benefits of microscopic FDIC over microscopic DIC particularly over surface roughening (twin) structures.

5.1. Microscopic in-situ FDIC and DIC (parallel) tensile loading experiment on as-cast Mg-AZ31

5.1.1. The procedure of the experiment

After checking the quality of the pattern with the method explained in section 3.2, the sample has been rendered ready for the experiment. The following are the implementation steps of the experiment

(i) The dimensions of the sample is carefully measured for engineering stress calculation.

(ii) The sample is placed in the loading frame and the screws are gradually tightened. The strain inadvertently applied to the sample during this stage reflects on the load cell and is occasionally relieved by repositioning the crosshead such that the load goes back to zero.

(iii) Both of the aligned cameras, their light sources in regular microscopy line and fluorescent microscopy line, controllers of the loading frame and the positioning stage are turned on.

(iv) Coordinate differences of two microscopy lines is measured. (A particular microscopic neighborhood selected in the gage section as a marker. The X-Y-Z positioner coordinates in each line, as the same point is positioned in the top left corner of an in-focus image, are recorded. The differential between these coordinates is determined as the coordinate translation between the two lines.) The accuracy of this step is crucial for the comparability of the DIC and FDIC results in corresponding images that should cover the same material neighborhood.

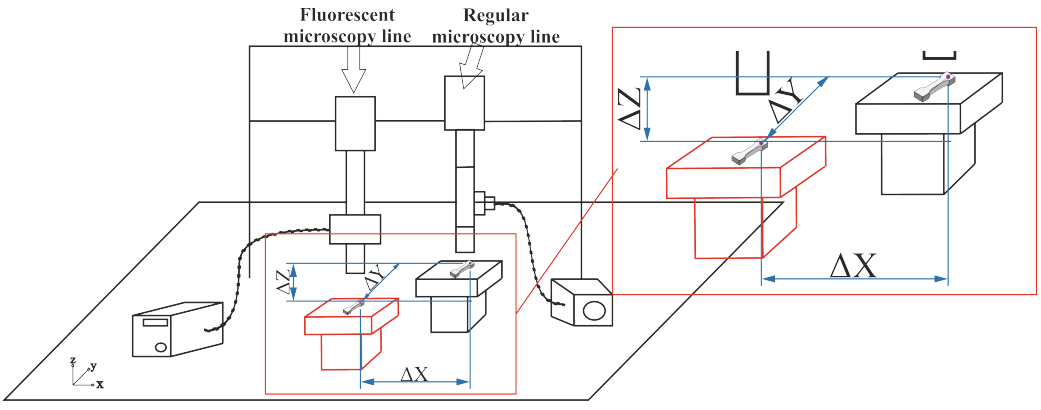

Figure 5.1. The coordinate difference between fluorescent microscopy line and regular microscopy line.

(v) Microscopic frames of interest (selected frames over the gage section) are identified in the regular microscopy line and the coordinates of them are recorded. The frames are selected in a 4x2 non-overlapping pattern. The position of the

frames under fluorescent microscopy line is calculated using the previous step's data. In this step, an important criterion is to keep the location of each frame sufficiently distant from each other. This is required so that exposing one frame under the FDIC line for imaging does not imply exposing the others unnecessarily. This way, photobleaching duration is reduced to only when it is necessary, namely, the imaging period of each frame. (See Figure 5.2.)

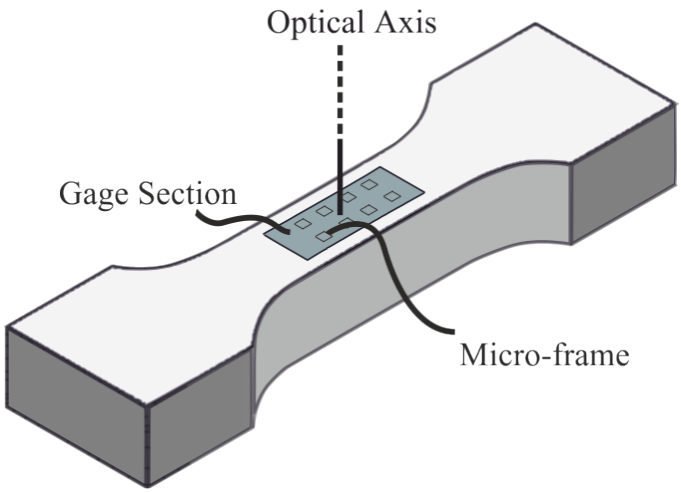

Figure 5.2. Micro frames specified on the gage section of the Mg-AZ31 dog-bone sample. The frames (in this case in a 4x2 pattern) are selected sufficiently distant to minimize photobleaching.

(vi) The micro-DIC and micro-FDIC images of the sample surface in the initial (undeformed) state of the sample is acquired. Focusing is done manually for each frame. For focusing the micro-FDIC images, the light source is switched to its lowest possible rate to maintain fluorescent effect for the actual imaging. When the image is focused, the incident light intensity is increased and the image is grabbed using Allied Visions's Vimba software.

(vii) The sample is loaded in position control using the control of the loading cell. Load is incremented in each load point until around 900 (N). Using a marker point, the shift in the frame coordinates are corrected. (It is crucial for DIC that the images stay on the same material points.)

(viii) The focusing and recording step before is repeated at each load point.

5.1.2. Stress-Strain Behavior

In our experiment with the as cast Mg-AZ31, the sample is subjected to a uniaxial tensile test. Figure 5.3 shows the stress-strain curve. *a* is the reference point in the experiment (undeformed). *b, c, d, e* are the load points in which fluorescent micro-DIC and regular micro-DIC images are collected.

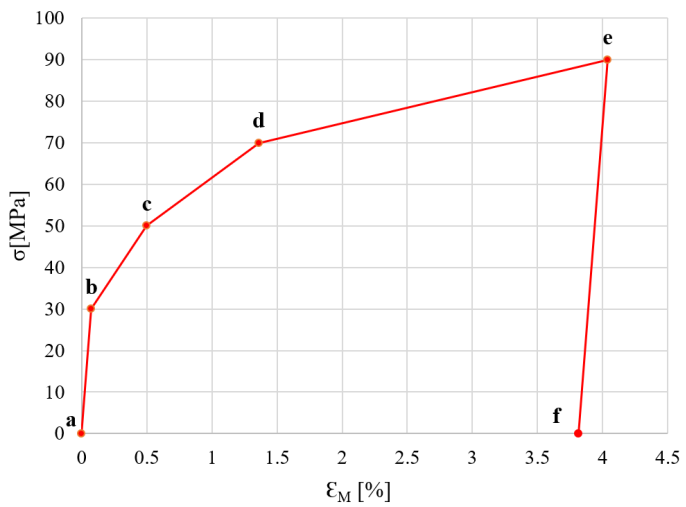

Figure 5.3. Stress-strain curve for Mg-AZ31 as-cast sample under uniaxial tension. Points *a, b, c, d, e* are the points at which micro-DIC and micro-FDIC images are collected. Point *a* serves as reference for load points *b*-*e*.

Here, the nominal strain ϵ_M in each load point, is given by

$$\epsilon_M = \overline{\epsilon}_{yy} \tag{5.1}$$

where $\overline{\epsilon}_{yy}$ is the average longitudinal strain in a representative frame. (Frames are large enough to constitute representative area elements. Frame averages agree within 2.5% for this sample.)

5.1.3. Microstructure evolution and comparison of DIC and FDIC imaging

Observation of the micro-images of the top surface, which are taken under regular microscopy line, reveals the topography of the sample during the deformation. The applied fluorescent pattern acts like a regular paint pattern without exposure to UV-light. The roughness of the surface caused by microstructural modifications (volumetric extrusions or intrusions) in increasing strain (Maximum ~ 4 % strain in this experiment), is apparent under regular DIC microscopy. Left side of the Figure 5.4 shows the micro-images of a frame during uniaxial tensile loading of as-cast Mg-AZ31 at all load points *a*-*e*. Red arrows indicate the twin bands activated on the surface at higher deformations. DIC invalidation and error potential is increased in these regions which are going to be discussed in section 5.1.5.

Right side of the Figure 5.4 shows the images grabbed from the FDIC line. Here, the speckles are produced by fluorescent emission of the nano-particles as it is excited with UV-light while all other frequencies are filtered by the filter cube. The distribution of the particles are roughly influenced by the initial surface topography and the DIC and FDIC images appear to be negatives of each other. While fluorescent regions appear white (high signal) under FDIC, they will scatter light as surface particles and appear dark under the regular DIC line. In summary, FDIC image can be somewhat affected from the initial surface topography and this cannot be avoided if one chooses the benefits of applying metallography to reveal grain boundaries after the polishing step. However, that just determines the initial distribution of fluorescent bead concentrations.

The main point, however, pertains to the (lack of) change in these patterns as the load is increased. While surface modifications appear in the DIC image at loads *d* and *e* , they do not show at all in the FDIC images. This means the initial premise of the study is actually satisfied. Since the micro-structure modifications are eliminated from the FDIC image, the DIC invalidations caused by them are not likely to happen in the FDIC analysis. (Details over comparative strain maps, are discussed in section

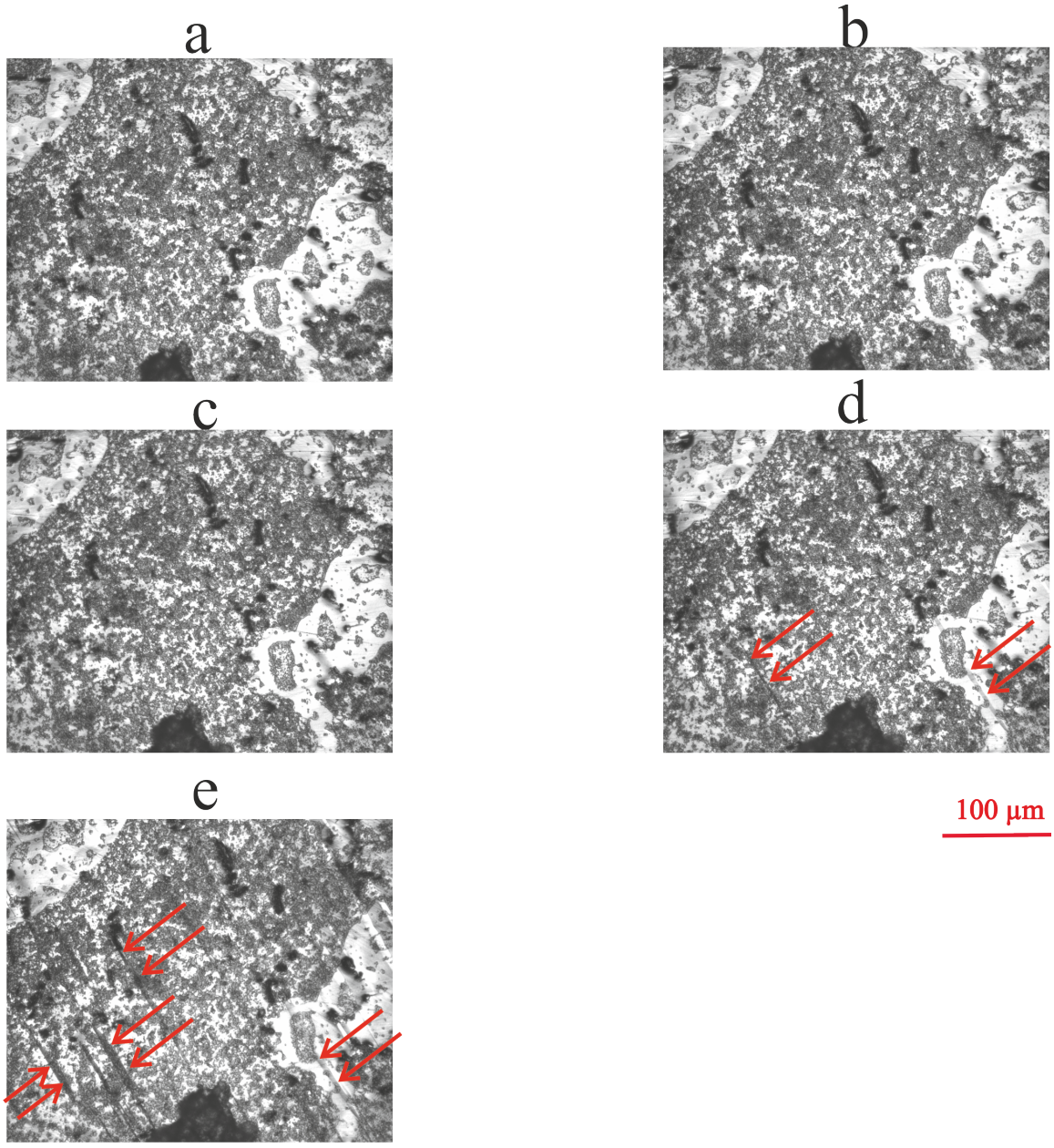

Figure 5.4. Micro-images of a DIC and FDIC frames during tensile loading in *a, b, c, d, e* load points in which the strain (ϵ_{yy}) is respectively equal to zero, 0.075%, 0.5%, 1.36%, 4.04%. Red arrows indicate twin bands , activated during the increasing loads causing surface roughening.

5.1.5.)

Figure 5.5 shows this more clearly over higher zoom images of two other frames at 4.04% strain (ϵ_{yy}). As evident on the DIC images, the material in these neighborhoods is deformed intensely, and the density of the twinned regions is quite high. FDIC micro-images, on the other hand, did perfectly omit the emergence of twins.

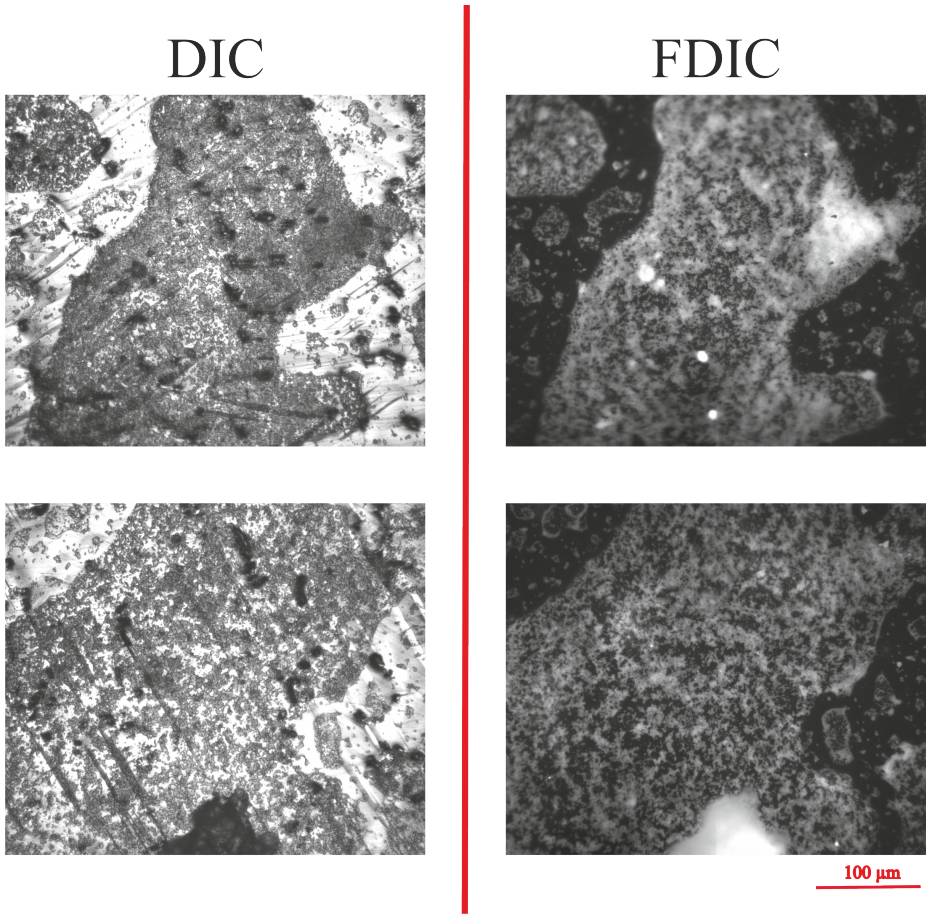

Figure 5.5. Micro-images of a DIC and FDIC frames during tensile loading in e load point with 4.04% strain (ϵ_{yy}). The micro-DIC images are representing the high density twinned regions while micro-FDIC images remain oblivious to the changes in microstructure.

5.1.4. Photobleaching rate in FDIC

In our first experiment on as-cast Mg-AZ31, with manual control of the light source to eliminate unnecessary exposure, the photobleaching has been reduced to approximately 1-7 % over the entire experiment. The focusing step is implemented by minimizing the UV-light intensity, which is sufficient to track the signal of the fluorescent particles. During the translation of the stage between frames, the light source is completely turned off. In the actual DIC image acquisition, the light source is switched up for sufficient intensity and dynamic range on the FDIC images. The intensity histograms of a selected micro-images over load points *a*-*e* are shown in Figure 5.6. As shown, the intensity histograms don't go through major changes, which means the fluorescent particles don't lose their fluorescence effect in the course of the experiment to any noticeable degree. Figure 5.7 is the diagram of mean intensity of load points that only show a limited decay of approximately 7% between points *a* and *b* . This amount is higher than the photobleaching rate in next load points that is approximately 1%. This complies with the exponential mechanism of photobleaching. Nevertheless, the strain maps (Section 5.1.5) will show that this limited amount of photobleaching does not effect the DIC analysis enough to cause errors and invalidations.

5.1.5. Analysis of Strain Maps

Microscopic DIC and FDIC analysis results of the experiment are represented in this section. In this experiment the pattern is applied with spray-gun and the fluorescent dye is a (1:10) concentration of 500 nm fluorescent nano-particles. The analysis for the tensile loading experiment on as-cast Mg-AZ31 is implemented in various regions of the micro-frames depending on the pattern quality which may be different because of the spottiness of the pattern applied with spray-gun on the sample surface. (In next experiment the pattern is applied with spin-caster which distributes the fluorescent particles more consistently and the full-frame DIC analyses will be possible.) The contour plots are used to show the distribution of strain in the

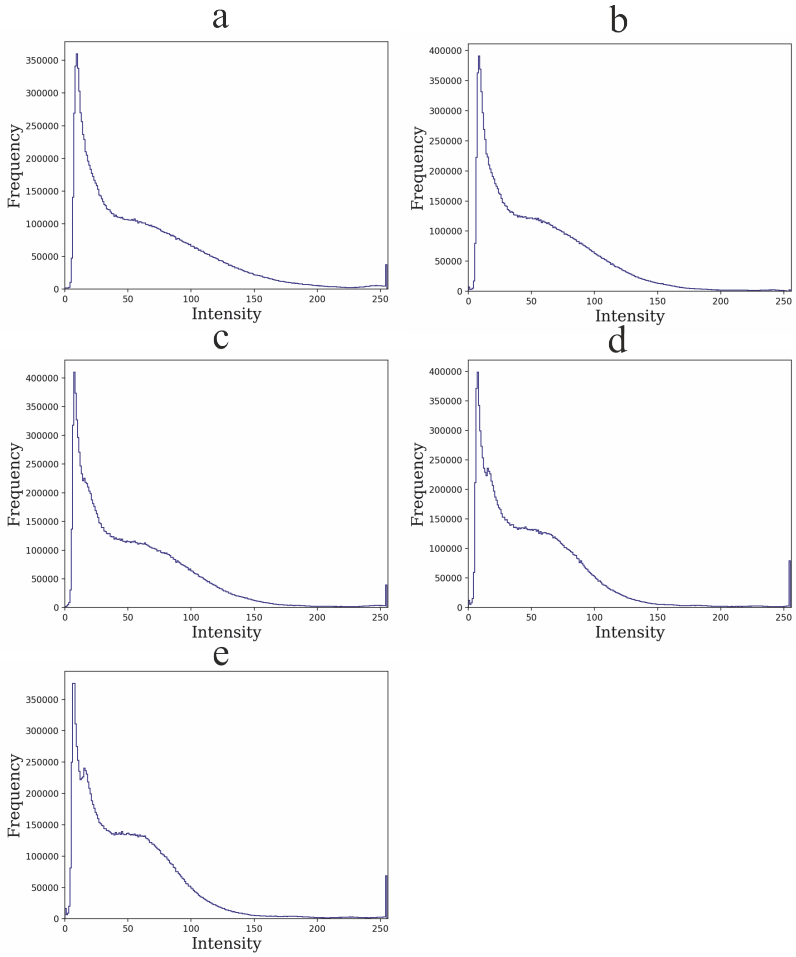

Figure 5.6. Intensity histograms of a micro-image over selected load points.

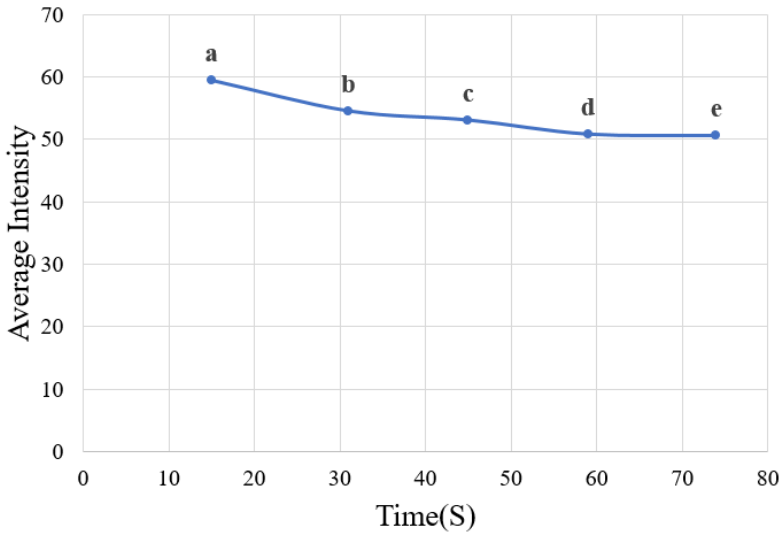

Figure 5.7. Photobleaching rate during the experiment over selected load points.

analysis grids. The contour plots of both DIC and FDIC analysis are presented on the individual micro-frames. Axial strain (ϵ_{yy}) is chosen as the contour plot variable.

For a representative analysis, a region with a potentially high quality pattern is selected on one of the material frames. Figure 5.8 shows this region imaged with both DIC and FDIC microscopy, marked with the DIC grid in each.

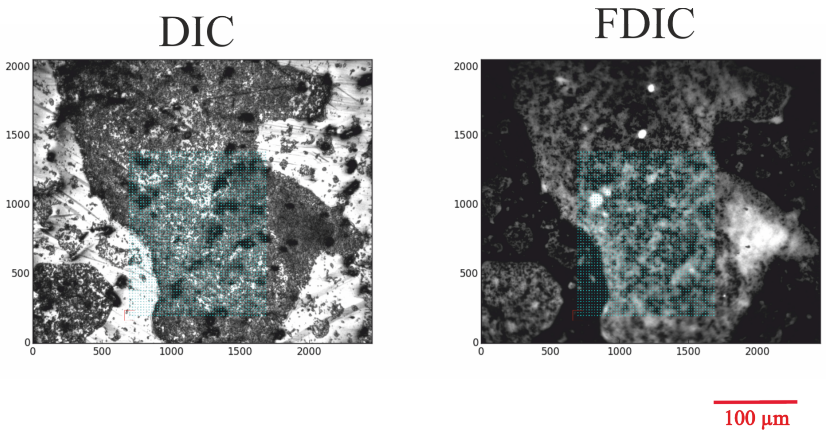

Figure 5.8. DIC and FDIC micro images and the analysis grids.

Local strain maps of DIC and FDIC analysis results are shown in Figure 5.9 zooming over the prescribed region. In the top row deformed images from both DIC an FDIC lines are shown. In this experiment, the material regions shifted significantly among load points and the attempted manual corrections were insufficient. (This is one of the improvement points in the next experiment.) Accordingly in the presented results of analysis, the strain maps could be correlated among subsequent points d and e and not with respect to the reference image whose material point coverage could not remain identical. However there is significant strain signal among the two points. As shown in Figure 5.3, the $\overline{\epsilon}_{yy}$ is 1.36% in d load point and 4.04% in e load point. Another issue that required improvement was manual focusing (through the Z adjustment of the stage) where visual judgment over images was employed instead of a calculated focus measure. This, severely hampered the comparability in some of the considered frames.

As shown in the DIC column of Figure 5.9, the strain contours (bottom) cover the entire region. Normally, this can give the wrong impression that the DIC analysis has been performed with no systematic errors. However, in the strain map for ϵ_{yy} in DIC microscopy, there is a region with an abnormal strain localization called false positive region. Focusing on DIC region, it is obvious that the region in which DIC fails to calculate ϵ_{yy} correctly is where twins have activated. However, not on the FDIC result shown on the right side of the Figure 5.9, the fields in this region still remain continuous and well-behaved. This is the first quantitative depiction of fluorescent microscopy working better in the twinned regions and avoiding the obvious errors of the regular microscopy DIC analysis in that neighborhood. Here, ϵ_{yy} is clearly more reliable as measured on the FDIC map.

Figure 5.10 shows a more extreme case where FDIC can provide robust strain measurement while DIC maps failed near entirely. In this case, the DIC and FDIC strain maps for ϵ_{yy} are analyzed at point d with $\overline{\epsilon}_{yy}$ is 1.36% compared to the initial reference, for a region of interest.

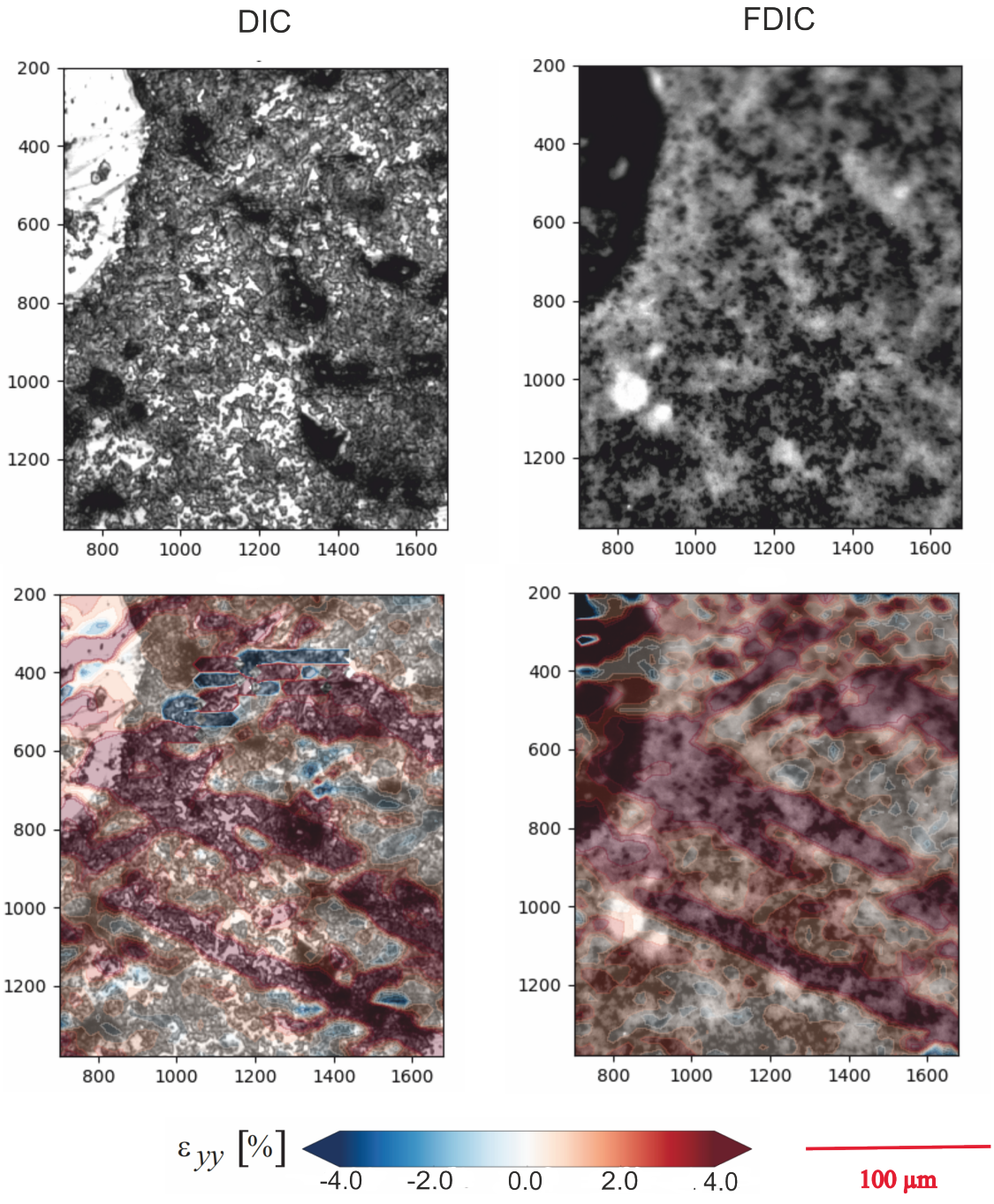

Figure 5.9. Micro-DIC and micro-FDIC images and results for ϵ_{yy} obtained for between load points d and e.

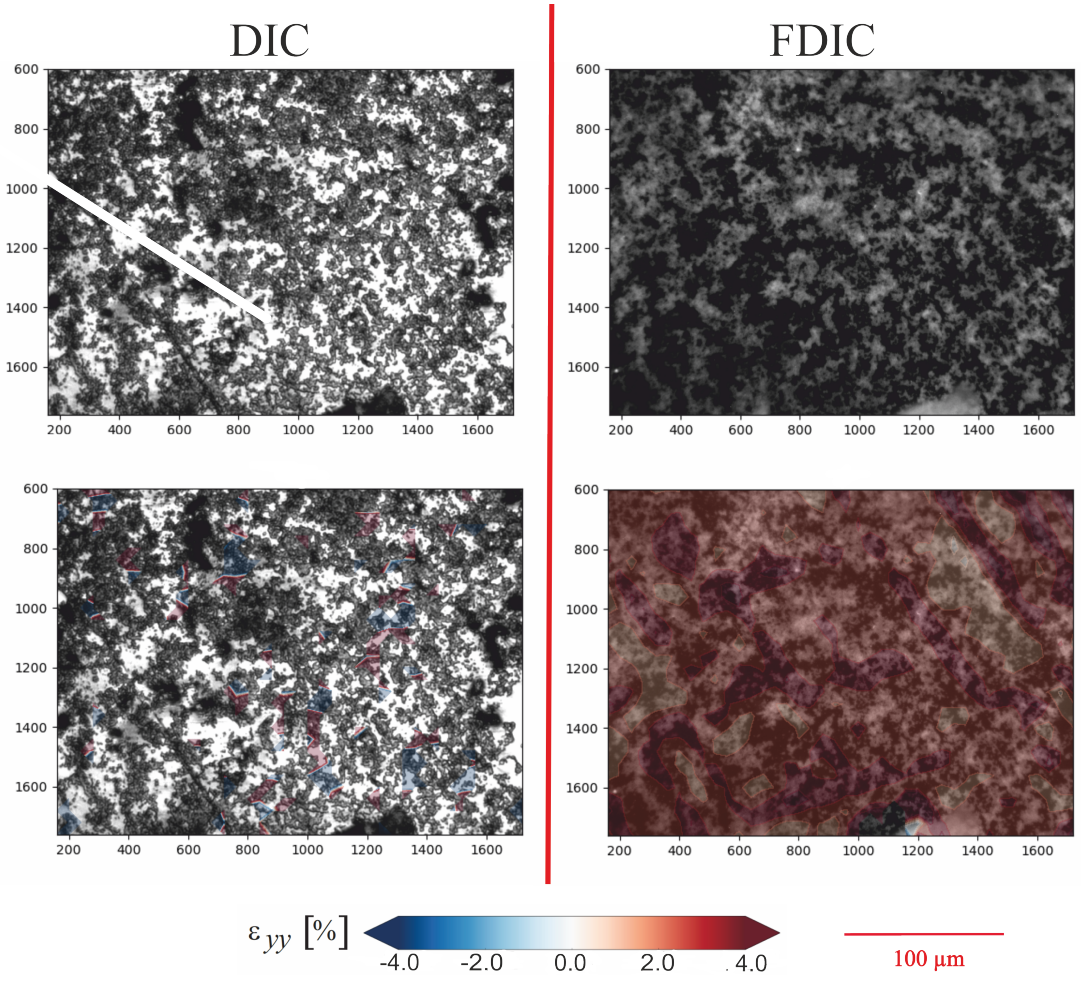

Figure 5.10. Micro-DIC and micro-FDIC frames and results for ϵ_{yy} obtained in load points *d*.

5.2. Microscopic in-situ FDIC and DIC (parallel) loading Experiments on Extruded Mg-AZ31

5.2.1. Developments for the procedure of the experiment

For the purpose of developing the procedure, some improvements are implemented in the procedure of this experiment for the extruded Mg-AZ31 experiment. The focus is on making the procedure more automated, reducing the manual steps with the aim of achieving time savings and more accurate image acquisition both in terms of locating material neighborhoods and focusing.

First of all, after choosing the intended micro-frames on the sample surface, the next calculations were done manually in the previous experiment and the motion of the stage was controlled manually, as well. However, in automated version of the procedure all the calculations are done at the beginning of the experiment once and for all. The coordinates and coordinate relations are inserted in a python script, and so the stage translations are controlled automatically throughout the experiment. This improvement is the most time-saving step of the new version of the procedure.

Another large improvement is auto-focusing. As said before, previously the focusing step was done manually. The manual focusing process not only requires more time that can be harmful for the photobleaching rate of the fluorescent nano-particles not to mention the inaccuracy of the human eye can be inaccurate. Here, sharper images are grabbed with the help of auto-focusing step that remain comparable among load points. Autofocusing is performed for a material locality when it is imaged both in regular microscopy and fluorescent microscopy lines. One of the advantages of this improvement is that in fluorescent microscopy line, with the help of the Fly Capture software of the camera and control of image grabbing properties e.g., shutter speed, exposure and gain of the camera, one can set the light source to the minimum available. In this case, computer calculation proved to have the ability to autofocus even with quite dark images. This reduced the photobleaching rate, which is going

to be discussed in section 5.2.4 for this experiment, to near zero.

Another important procedural development pertained to the capability to stay on the same material regions at each load. For this an auto-locating function has been coded. Auto-locating step is implemented only for regular microscopy line: In the reference state (first load point) where there is no deformation, the micro-images are taken. In the next load point, the micro-images are auto focused and grabbed. Then, the auto-locator script is run and the relative displacement between material points is calculated through a fast ORB algorithm. This displacement is fed back to the positioning stage to move the frame to the original neighborhood of the material points. Auto-locating is implemented individually at each one of the 8 selected frames and translation of each frame is independently determined and corrected. Auto-locating is not implemented under the FDIC line since the translation between two lines is predetermined. So correcting the position of a frame under one line is sufficient except for stage errors which typically remain under 2 μm, essentially ignorable.

The only manual step of the experiment is the control of the UV-light source which is still being switched off during the motion of the positioning stage kept at very low setting during focusing and switching up during the image grab for achieving high intensity micro-images under fluorescent microscopy. In this experiment, however, with the better cameras, the UV intensity never had to be maximized even during imaging and kept at the 2nd setting out of 4. This certainly helped with the very low photobleaching rates.

5.2.2. Stress-Strain Behavior

In the experiment on extruded Mg-AZ31, the sample is subjected to a compression loading test. This is in contrast to the tensile loading for the as-cast sample. The difference is that the extruded sample has a very sharp forming texture and while compression along the extrusion axis activates profuse twinning, tension does not. Since this study is after the benefits of FDIC during heavy twinning, the problematic

compression direction was opted. Figure 5.11 is the stress-strain curve of the experiment. Micro DIC and FDIC analysis are done in greater detail at 17 load points. (Shown on curve from *a* to *q*.) As shown on the figure, the sample is loaded until -4% strain and it is unloaded after load point *p*. In load points which are in high strain regions, the activated twins are obvious on the sample surface which are going to be explained in the next section.

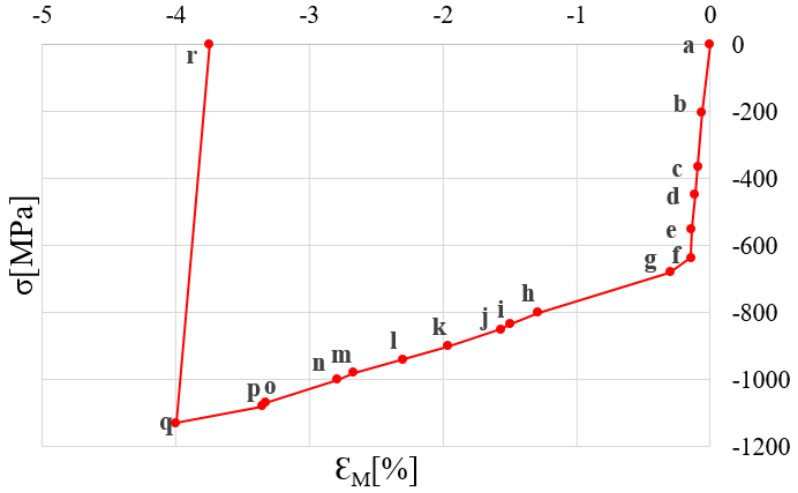

Figure 5.11. Stress-strain curve for Mg-AZ31 extruded sample. The sample is subjected to uniaxial compression from a reference state (*a*) and then it is unloaded (*r*). Points *b*-*r* are the load points in which micro-DIC and micro-FDIC images are collected.

5.2.3. Microstructure evolution and comparison of DIC and FDIC imaging

By taking all the mentioned discussions in section 5.1.3 in to consideration, the micro-structural progress during the compression loading experiment on extruded batch of Mg-AZ31 is represented in Figure 5.12 The progressive formation of twin activities on the surface of the sample in increasing ϵ_{yy} can be easily observed in the micro-images of the regular microscopy. (Shown on the left side of the Figure 5.12.) Red arrows are indicating the twin bands activated in load point *j, m, q*. It is observed on the micro-images that the twin bands are getting wider and sharper at higher deformations. Some of these twin bands in high strain load points are causing

volumetric modifications. DIC invalidations and error potential is increased in these regions. (See section 5.2.5)

The results here, are almost identical with the results discussed in Section 5.1.3.

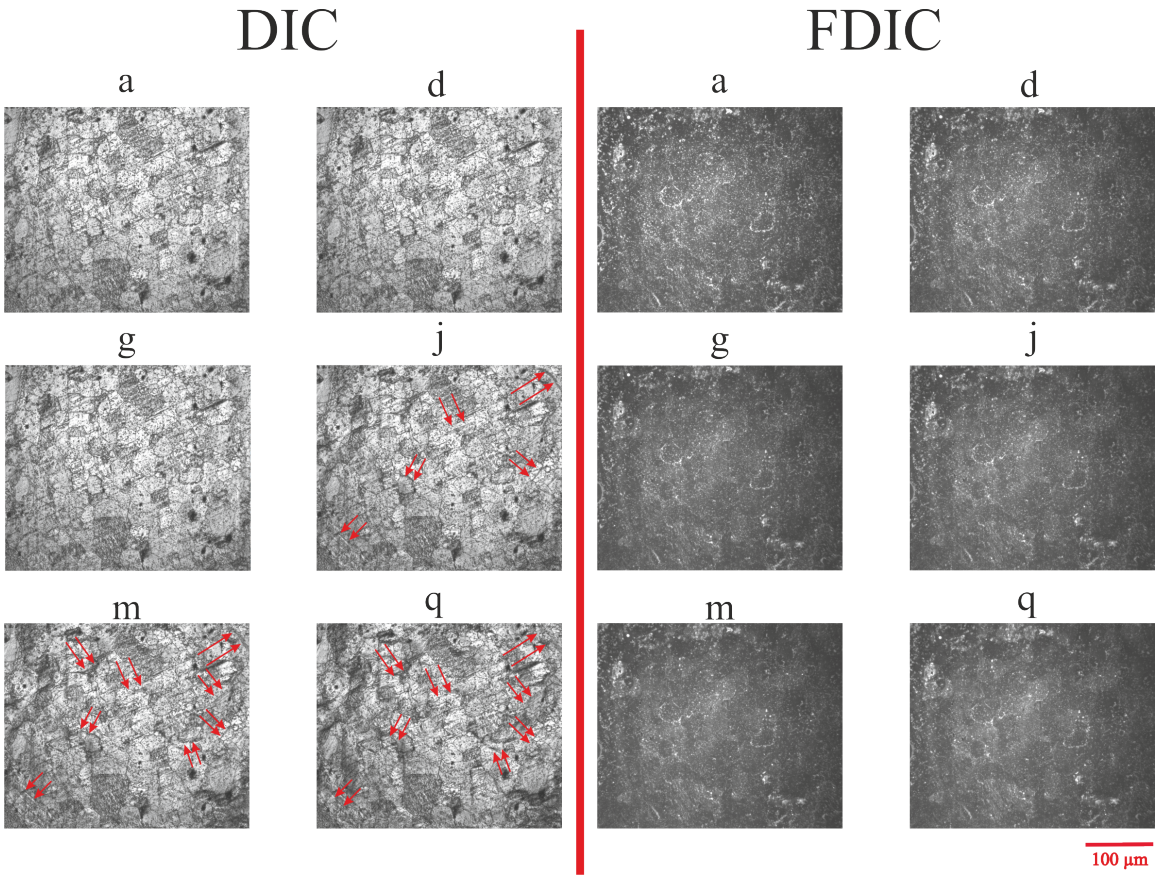

Figure 5.12. DIC and FDIC micro-images of a frames during compression loading in *a, d, g, j, m, q* load points in which the strain (ϵ_{yy}) is respectively equal to zero, -0.113%, -0.145%, -1.57%, -2.67%, -4%. Red arrows indicate twin bands activated during the increasing loads.

Figure 5.13 is showing two different micro-images in both regular and fluorescent microscopy lines in this experiment. The frames are from load point k that ϵ_{yy} equals to approximately -2%. The highly deformed surface with the obvious microstructural modifications of the sample is shown in the right side of the figure while the left side of the figure represents the FDIC t micro-images in which the emergence of the twins

on the surface is not apparent.

5.2.4. Photobleaching rate in FDIC

In the second experiment on the extruded Mg-AZ31 sample, as explained in section 5.2.1, the procedure is more automated. Therefore, the emission from the fluorescent particles (FDIC pattern) is more robust and the photobleaching rate is reduced to 1%. To detail the procedural improvements, first, the image grabbing step is implemented more quickly and the second, the newer Flir cameras are more efficient in dark environments. The high signal to noise ratio of these cameras allow even seemingly dark images to be analyzed for relative focus measure. Hence, auto-focusing could be implemented with the lowest setting of the UV light incident intensity. As UV-light exposure is reduced both at imaging and focusing stages, and the sample is never exposed to the most intense setting of the UV light source, photobleaching rate is reduced significantly.

The intensity histograms of the FDIC micro-images in Figure 5.12 are shown in Figure 5.14. These depict that the loss in fluorescent emission is very limited.

Figure 5.15 is the diagram of mean intensity of a FDIC micro-image all the load points *a*-*r*. The diagram shows that, there is only a limited decay of fluorescence effect of the particles between points *a*-*e* by approximately 3% (less than the previous experiment in its first load points.) During the rest of the load points, intensity decay is as low as 0.1%. Hence, with the improvements in the procedure, even the limited degree of intensity decay observed in the previous experiment is remedied.

5.2.5. Analysis of Strain Maps

Microscopic DIC and FDIC analysis results of the second experiment are represented in this section. The fluorescent dye which is a (1:10) concentration of 500 nm fluo-beads in water, is applied with a spin-caster. Compared to the spray-gun

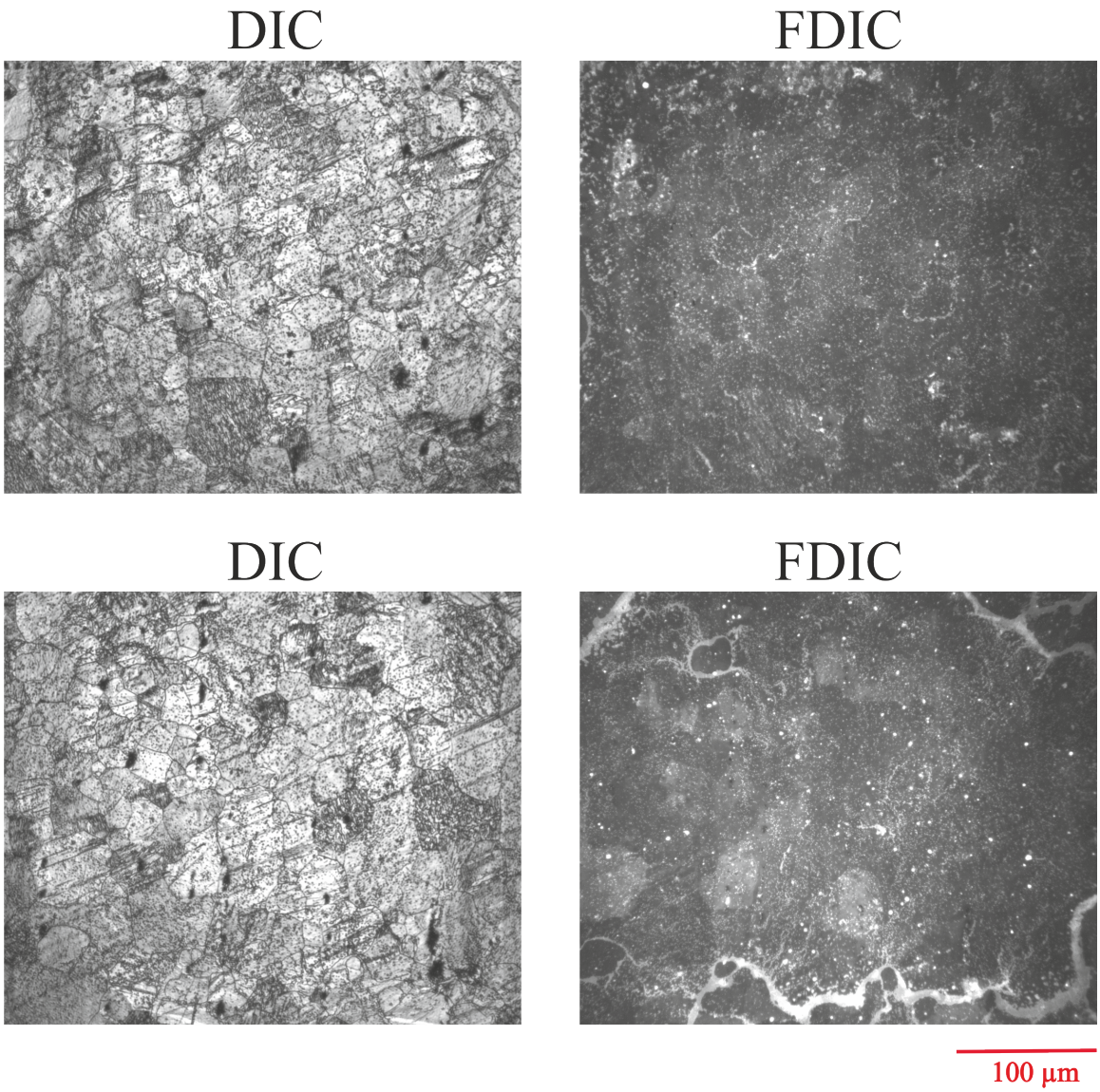

Figure 5.13. Micro-images of a DIC and FDIC frames during compression loading in k load point with -2% strain (ϵ_{yy}). The micro-DIC images are representing the high density twinned regions while micro-FDIC images are independent from the microstructural changes.

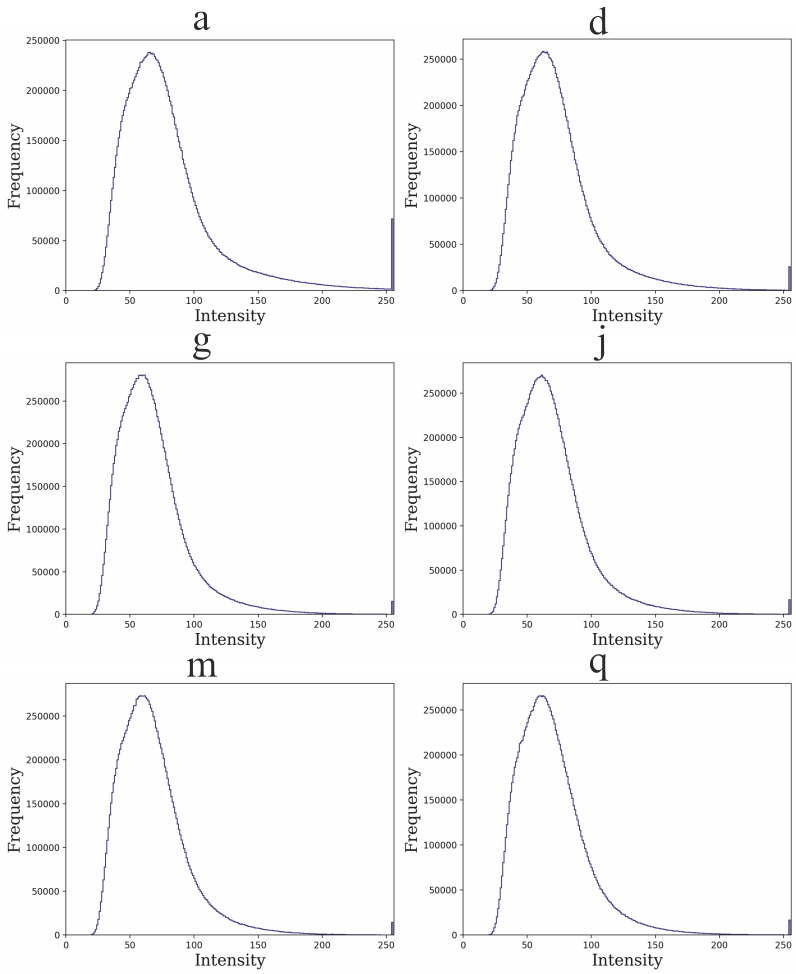

Figure 5.14. Intensity histograms of the micro-images in *a, d, g, j, m, q* load points.

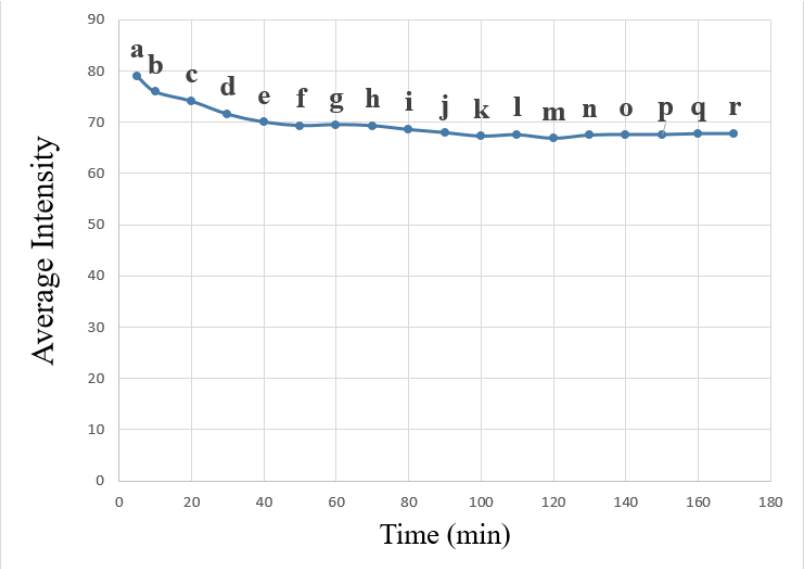

Figure 5.15. Photobleaching rate during the experiment in load points *a-r*.

application of the previous experiment, spin-caster spreads the fluorescent dye on the sample surface more consistently. The sample surface is coated in a way that all the chosen micro-frames have consistent patterns with sufficient intensity signature all over the field. Consequently, there is no need for local grids (i.e., restricting the grids to regions where DIC pattern is adequate) and full frame grids are applied for DIC and FDIC analysis. Accordingly, the provided contour plots will represent full-frame DIC and FDIC analysis results.

For a more comprehensive understanding and discussing of the results, transverse strain, ϵ_{xx}, and in-plane rotation, ω_{xy}, are also considered alongside the axial strain ϵ_{yy}. The physics of how the combined interpretation of these parameters lead to the orientations of plasticity structures is presented in Figure 5.16. Plasticity mechanisms (twinning or slip) and their cumulative active create simple shear. Figure 5.16 shows the two extremes regarding the activity orientation of the simple shear. As shown in parts (a) and (b) of the figure, if the plane of shear of the localization structure coincides exactly with the observation plane (x-y), then $\epsilon_{yy} = -\epsilon_{xx}$ will apply yielding a local Poisson's ratio (ν) of 1. In addition, the rotation that is associated

with the simple shear will reflect in full measure to the maps. Conversely, if shear runs in or out of the plane (Figure 5.16(c)), no contraction occurs on the observation plane, yielding $\epsilon_{xx} = \nu = 0$. These bands typically appear as flat bands on the surface and create surface extrusions and intrusions. In short, in-plane bands will be identified as those that appear in maps of all ϵ_{yy}, ϵ_{xx}, and ω_{xy}, while out-of-plane bands will be discerned as those that appear in ϵ_{yy} but do not reflect in both ϵ_{xx}, and ω_{xy} maps. Since, extrusions/intrusions are associated with DIC failure, the attention will be on spotting a correlation between DIC invalidations and out-of-plane shear activity.

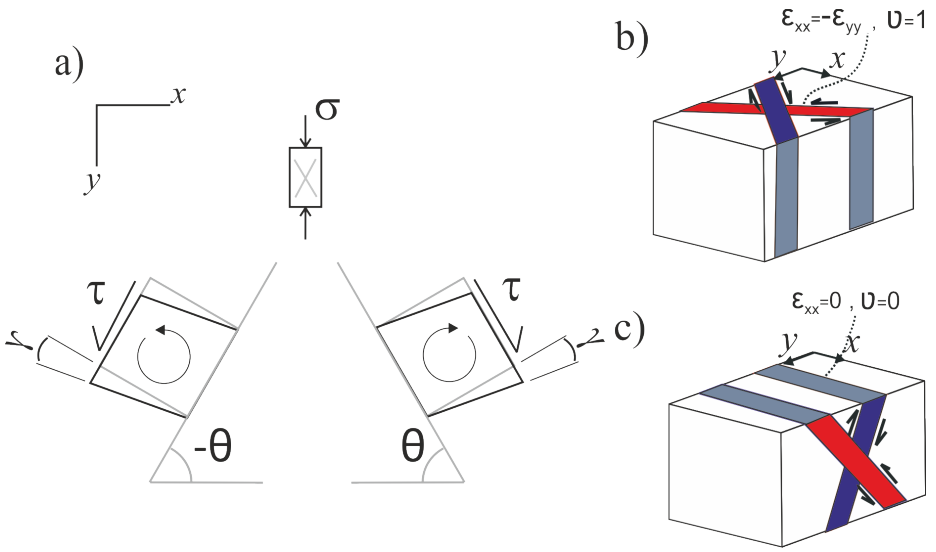

Figure 5.16. a) the ideal simple shear structures on the s-y plane on a saple that is under compression loading. b) sketch for shear band Poisson's ratio when its plane of shear is x-y (top surface). c) sketch foe shear band Poisson's ration when it's plane of shear is y-z (side surface)

Figure 5.17 represents DIC and FDIC analysis results of a chosen frame over selected load points *j, k, l, m, n, o* where average ϵ_{yy} is -1.57%, -1.96%, -2.3%, -2.67%, -2.79%, -3.33%, respectively. DIC (left) and FDIC (right) results are paired comparatively in as the main two columns of the figure. The corresponding micrographs are provided at the top two rows of Figure 5.17, below which ϵ_{yy}, ϵ_{xx} and ω_{wxy} maps are presented. For all the micro-images (specially in the further load points),

DIC invalidations appear as missing data points on the contour plots in the DIC analysis while invalidations are absent in the FDIC maps. So, firstly, one notes that, the main premise of the study (robust strain measurement of deformation roughened surface) is satisfied.

As shown in the DIC column of Figure 5.17, the contour plots of ϵ_{yy} have regions with abnormal strain localization. With a closer examination over ϵ_{yy} plots, it is evident that the invalidations are occured on the flat bands. Since these bands don't appear on the ϵ_{xx} and ω_{xy}, they are found to be out-of-plane shear structures. To present this aspect with clarity, Figure 5.18 depicts both DIC and FDIC analysis results of the micro-frame shown on Figure 5.17 in load point h in which the ϵ_{yy} is equal to -1.29%. The strain data for the obvious invalidation region that is circled in the DIC maps, is available in the FDIC maps. This invalidation region corresponds to a band that has the clear characteristics of out-of-plane shear activity, namely, it is largely absent in transverse strain and rotation maps.

To identify the differences in FDIC and DIC results in more detail, the analysis of this experiment is also done quantitatively. For this purpose, ϵ_{yy} and ϵ_{xx} histograms are provided. At this load point, strains at localization bands are significantly higher than the average value. The logarithmic histograms are provided for providing a more accurate depiction of the extreme strain points, as well as statistical outliers. It is quite evident that logarithmic histograms that are in the DIC column in the Figure 5.18 contain more outliers than the logarithmic histograms in the FDIC column. The relative absence of outlier data points again speaks to the added robustness of the FDIC measurement. Figure 5.19 is the DIC and FDIC analysis result of the same frame in the same load point (h) but in a close-up about the discussed DIC invalidation. Through the utilization of this limited region, the histogram comparison yields the benefit of FDIC with more clarity.

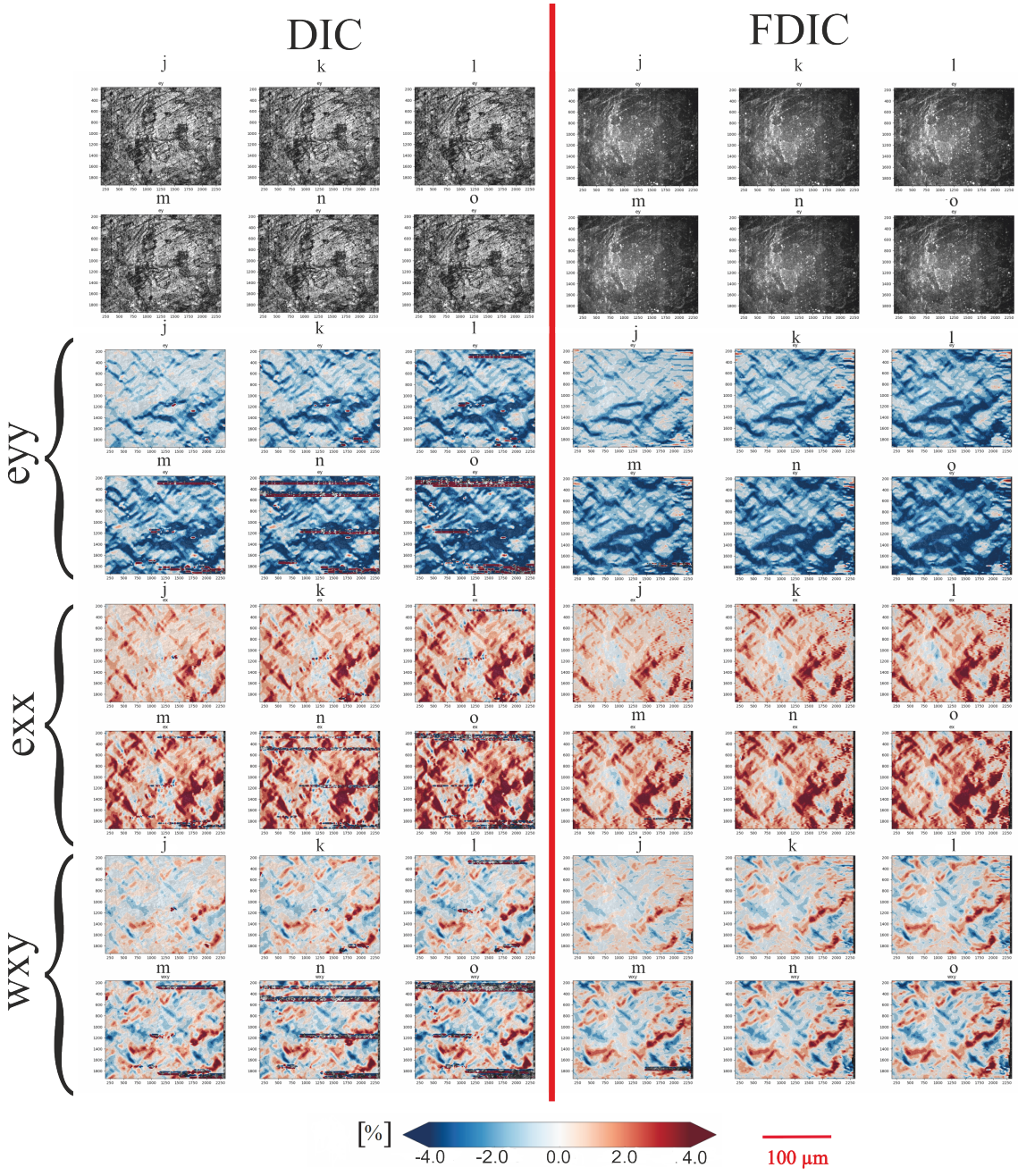

Figure 5.17. Micro-DIC and micro-FDIC images and results for ϵ_{yy}, ϵ_{xx} and ω_{wxy} obtained for the load points *j, k, l, m, n, o*. Invalidations are observed in DIC analysis results while FDIC results are continuous and well-behaved.

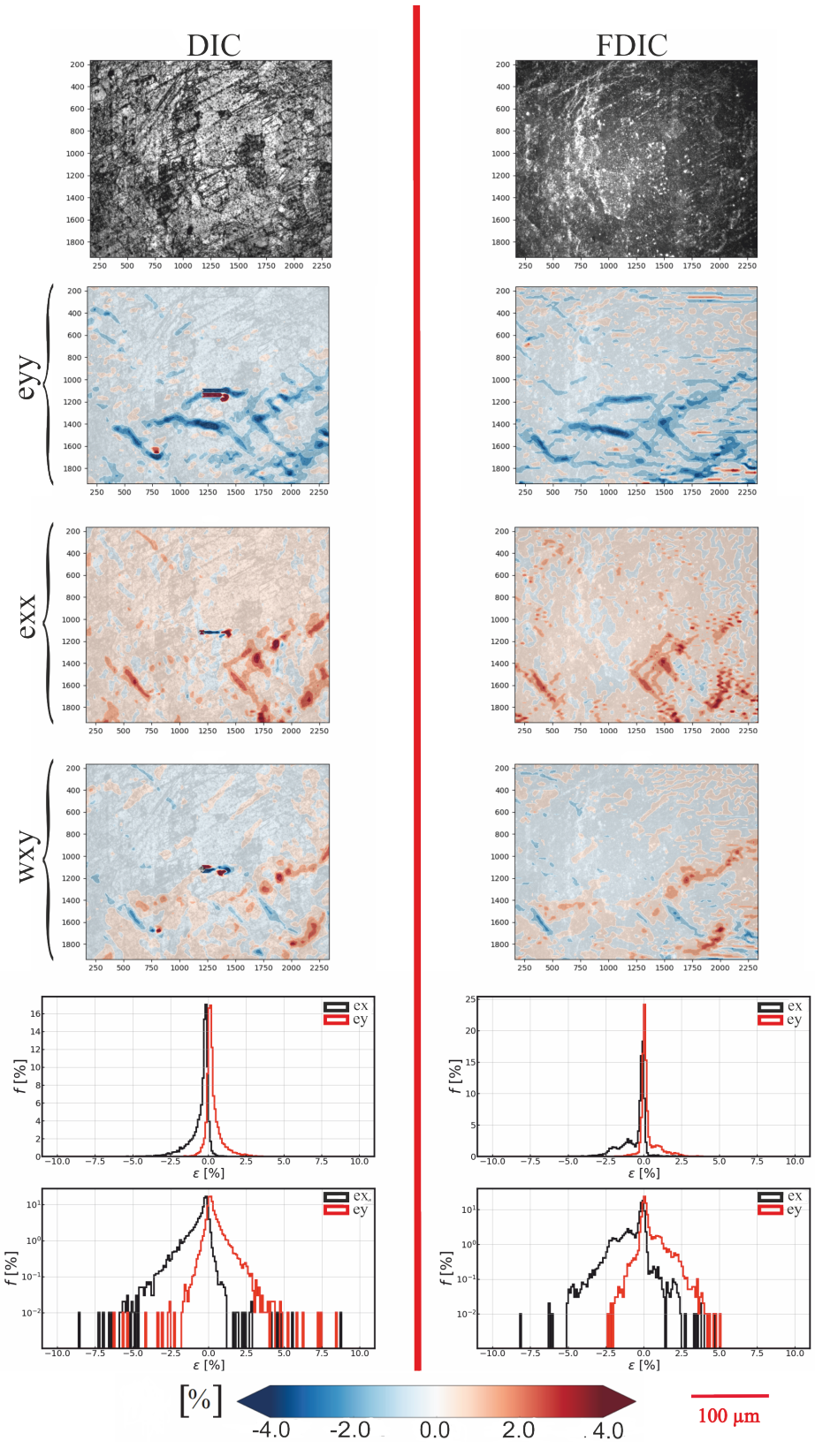

Figure 5.18. Micro-DIC and micro-FDIC images and results for ϵ_{yy}, ϵ_{xx} and ω_{wxy} obtained for the load point h.

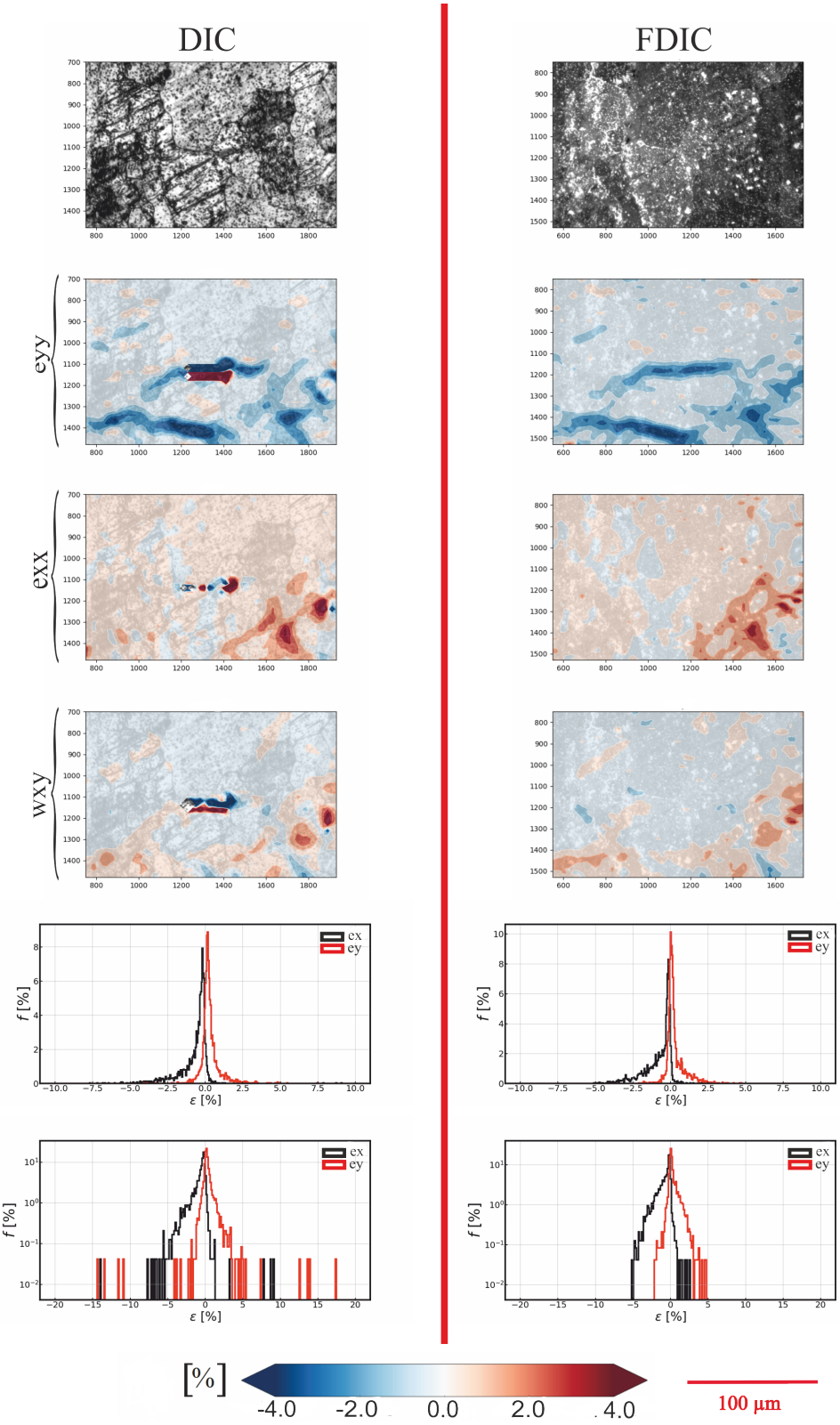

Figure 5.19. Micro-DIC and micro-FDIC images and results for ϵ_{yy}, ϵ_{xx} and ω_{wxy} obtained for the load point h in a smaller grid around a region with DIC invalidation.

6. CONCLUSION

Fluorescent digital image correlation (FDIC) is applied on a Mg-AZ31 alloy that suffers from DIC invalidation due to twin emergence, as robust strain measurement strategy. A tension test on as-cast sample of Mg-AZ31 and, later, a compression test on annealed extruded sample of Mg-AZ31 have been the two experiments that were considered. The second experiment is formulated over the experiences of the first experiment. The sample surface is observed with both regular and fluorescent optical microscopy lines in these experiments for comparative evaluation of the FDIC benefits. Deformation maps are measured with digital image correlation and the fluorescent digital image correlation.

An important stage of the study is the proper application of the fluorescent DIC pattern. Fluorescent beads have been determined to be the preferred base material over mere solutions. Bead solutions are applied over the surface with a spray gun in the first experiment and with a spin-caster in the second experiment. High quality patterns (monodisperse, isotropic and high contrast) have been produced particularly with spin casting. The results show that the premise of the FDIC method is viable, namely, while twins visibly emerged in the regular DIC images as load is progressed, they were absent in the FDIC images as intended. In accordance, while DIC is invalidated in certain twinned material neighborhoods, FDIC maintains producing consistent results.

7. FUTURE WORK

In this thesis, fluorescent digital image correlation is implemented locally in the frames selected on the surface. As a future work, a full-field microscopic strain measurement can be implemented since photobleaching could be minimized with the final refinements on the procedure and the equipment. This will lead to a comprehensive understanding of deformation fields of the samples, e.g, as-cast Mg-AZ31 sample. In this case, the grains are larger than the frame size; and only with a full-field analysis, it can be possible to observe statistically-significant number of grains.

The UV-light intensity on the sample surface to excite the fluorescent particles is still manually controlled to avoid the photobleaching phenomenon in our experiments. In the future, a completely automated experiment can be formulated with an improved light source where the UV-light intensity is also computer controlled.

Most importantly, the method can be implemented on other material/load configurations that exhibit a high density of DIC invalidation on the sample surface due to roughening.

REFERENCES

1. Peters, W. and W. Ranson, "Digital imaging techniques in experimental stress analysis", *Optical engineering*, Vol. 21, No. 3, p. 213427, 1982.

2. Sutton, M. A., J. J. Orteu and H. Schreier, *Image correlation for shape, motion and deformation measurements: basic concepts, theory and applications*, Springer Science & Business Media, 2009.

3. Kang, J., M. Jain, D. Wilkinson and J. Embury, "Microscopic strain mapping using scanning electron microscopy topography image correlation at large strain", *The Journal of Strain Analysis for Engineering Design*, Vol. 40, No. 6, pp. 559–570, 2005.

4. Scrivens, W., Y. Luo, M. A. Sutton, S. Collette, M. L. Myrick, P. Miney, P. Colavita, A. P. Reynolds and X. Li, "Development of patterns for digital image correlation measurements at reduced length scales", *Experimental Mechanics*, Vol. 47, No. 1, pp. 63–77, 2007.

5. Jin, H., W. Lu and J. Korellis, "Micro-scale deformation measurement using the digital image correlation technique and scanning electron microscope imaging", *The Journal of Strain Analysis for Engineering Design*, Vol. 43, No. 8, pp. 719–728, 2008.

6. Orozco-Caballero, A., D. Lunt, J. D. Robson and J. Q. da Fonseca, "How magnesium accommodates local deformation incompatibility: a high-resolution digital image correlation study", *Acta Materialia*, Vol. 133, pp. 367–379, 2017.

7. Beaudoin, A., J. Bryant and D. A. Korzekwa, "Analysis of ridging in aluminum auto body sheet metal", *Metallurgical and Materials Transactions A*, Vol. 29, No. 9, pp. 2323–2332, 1998.

8. Sachtleber, M., Z. Zhao and D. Raabe, "Experimental investigation of plastic grain interaction", *Materials Science and Engineering: A*, Vol. 336, No. 1-2, pp. 81–87, 2002.

9. Efstathiou, C., H. Sehitoglu and J. Lambros, "Multiscale strain measurements of plastically deforming polycrystalline titanium: role of deformation heterogeneities", *International Journal of Plasticity*, Vol. 26, No. 1, pp. 93–106, 2010.

10. Barkia, B., V. Doquet, E. Héripré and I. Guillot, "Characterization and analysis of deformation heterogeneities in commercial purity titanium", *Materials Characterization*, Vol. 108, pp. 94–101, 2015.

11. Padilla, H., J. Lambros, A. Beaudoin and I. Robertson, "Relating inhomogeneous deformation to local texture in zirconium through grain-scale digital image correlation strain mapping experiments", *International Journal of Solids and Structures*, Vol. 49, No. 1, pp. 18–31, 2012.

12. Marya, M., L. G. Hector, R. Verma and W. Tong, "Microstructural effects of AZ31 magnesium alloy on its tensile deformation and failure behaviors", *Materials science and engineering: A*, Vol. 418, No. 1-2, pp. 341–356, 2006.

13. Martin, G., C. W. Sinclair and J.-H. Schmitt, "Plastic strain heterogeneities in an Mg–1Zn–0.5 Nd alloy", *Scripta Materialia*, Vol. 68, No. 9, pp. 695–698, 2013.

14. Aydiner, C. C. and M. A. Telemez, "Multiscale deformation heterogeneity in twinning magnesium investigated with in situ image correlation", *International Journal of Plasticity*, Vol. 56, pp. 203–218, 2014.

15. Uçar, S., *Grain size dependence of twin-dominant deformation in rolled magnesium AZ31 investigated by in situ microscopic image correlation*, Master's Thesis, bogazici univesity, 2017.

16. Kapan, E., N. Shafaghi, S. Ucar and C. C. Aydiner, "Texture-dependent charac-

ter of strain heterogeneity in Magnesium AZ31 under reversed loading", *Materials Science and Engineering: A*, Vol. 684, pp. 706–711, 2017.

17. Hazeli, K., J. Cuadra, F. Streller, C. Barr, M. Taheri, R. Carpick and A. Kontsos, "Three-dimensional effects of twinning in magnesium alloys", *Scripta Materialia*, Vol. 100, pp. 9–12, 2015.

18. Yan, D., C. C. Tasan and D. Raabe, "High resolution in situ mapping of microstrain and microstructure evolution reveals damage resistance criteria in dual phase steels", *Acta Materialia*, Vol. 96, pp. 399–409, 2015.

19. Berfield, T. A., J. K. Patel, R. G. Shimmin, P. V. Braun, J. Lambros and N. R. Sottos, "Fluorescent image correlation for nanoscale deformation measurements", *Small*, Vol. 2, No. 5, pp. 631–635, 2006.

20. Sakakibara, J., K. Hishida and M. Maeda, "Vortex structure and heat transfer in the stagnation region of an impinging plane jet (simultaneous measurements of velocity and temperature fields by digital particle image velocimetry and laser-induced fluorescence)", *International Journal of Heat and Mass Transfer*, Vol. 40, No. 13, pp. 3163–3176, 1997.

21. Snyder, A. P., D. B. Greenberg and P. V. Scarpino, "Viable microorganism detection by induced fluorescence", Feb. 18 1992, uS Patent 5,089,395.

22. Bruck, H., S. McNeill, M. A. Sutton and W. Peters, "Digital image correlation using Newton-Raphson method of partial differential correction", *Experimental mechanics*, Vol. 29, No. 3, pp. 261–267, 1989.

23. Zipperian, D. C., "Metallographic specimen preparation basics", *Pace technology*, 2001.

24. Berfield, T., J. Patel, R. Shimmin, P. Braun, J. Lambros and N. Sottos, "Micro- and nanoscale deformation measurement of surface and internal planes via digital

image correlation", *Experimental Mechanics*, Vol. 47, No. 1, pp. 51–62, 2007.

25. Scrivens, W., Y. Luo, M. A. Sutton, S. Collette, M. L. Myrick, P. Miney, P. Colavita, A. P. Reynolds and X. Li, "Development of patterns for digital image correlation measurements at reduced length scales", *Experimental Mechanics*, Vol. 47, No. 1, pp. 63–77, 2007.

26. Collette, S., M. Sutton, P. Miney, A. Reynolds, X. Li, P. Colavita, W. Scrivens, Y. Luo, T. Sudarshan, P. Muzykov *et al.*, "Development of patterns for nanoscale strain measurements: I. Fabrication of imprinted Au webs for polymeric materials", *Nanotechnology*, Vol. 15, No. 12, p. 1812, 2004.

27. Van Blaaderen, A. and A. Vrij, "Synthesis and characterization of colloidal dispersions of fluorescent, monodisperse silica spheres", *Langmuir*, Vol. 8, No. 12, pp. 2921–2931, 1992.

28. Song, L., E. Hennink, I. T. Young and H. J. Tanke, "Photobleaching kinetics of fluorescein in quantitative fluorescence microscopy.", *Biophysical journal*, Vol. 68, No. 6, p. 2588, 1995.

29. Young, R. M., J. K. Arnette, D. A. Roess and B. G. Barisas, "Quantitation of fluorescence energy transfer between cell surface proteins via fluorescence donor photobleaching kinetics", *Biophysical journal*, Vol. 67, No. 2, pp. 881–888, 1994.

30. Axelrod, D., D. Koppel, J. Schlessinger, E. Elson and W. W. Webb, "Mobility measurement by analysis of fluorescence photobleaching recovery kinetics", *Biophysical journal*, Vol. 16, No. 9, pp. 1055–1069, 1976.

31. Kubitscheck, U., M. Kircheis, R. Schweitzer-Stenner, W. Dreybrodt, T. Jovin and I. Pecht, "Fluorescence resonance energy transfer on single living cells. Application to binding of monovalent haptens to cell-bound immunoglobulin E", *Biophysical journal*, Vol. 60, No. 2, pp. 307–318, 1991.

32. Peters, R., A. Brünger and K. Schulten, "Continuous fluorescence microphotolysis: A sensitive method for study of diffusion processes in single cells", *Proceedings of the National Academy of Sciences*, Vol. 78, No. 2, pp. 962–966, 1981.

33. Langer, H., *Biochemistry and Physiology of Visual Pigments: Symposium Held at Institut für Tierphysiologie, Ruhr-Universität Bochum/W. Germany, August 27–30, 1972*, Springer Science & Business Media, 2012.